

Enzyme promiscuity drives branched-chain fatty acid synthesis in adipose tissues

Martina Wallace¹, Courtney R. Green¹ , Lindsay S. Roberts², Yujung Michelle Lee^{3,4}, Justin L. McCarville³, Joan Sanchez-Gurmaches^{5,6}, Noah Meurs¹, Jivani M. Gengatharan¹, Justin D. Hover¹, Susan A. Phillips⁷, Theodore P. Ciaraldi^{8,9}, David A. Guertin¹⁰, Pedro Cabrales¹, Janelle S. Ayres³, Daniel K. Nomura², Rohit Loomba¹¹ and Christian M. Metallo^{1,12,13*}

Fatty acid synthase (FASN) predominantly generates straight-chain fatty acids using acetyl-CoA as the initiating substrate. However, monomethyl branched-chain fatty acids (mmBCFAs) are also present in mammals but are thought to be primarily diet derived. Here we demonstrate that mmBCFAs are de novo synthesized via mitochondrial BCAA catabolism, exported to the cytosol by adipose-specific expression of carnitine acetyltransferase (CrAT), and elongated by FASN. Brown fat exhibits the highest BCAA catabolic and mmBCFA synthesis fluxes, whereas these lipids are largely absent from liver and brain. mmBCFA synthesis is also sustained in the absence of microbiota. We identify hypoxia as a potent suppressor of BCAA catabolism that decreases mmBCFA synthesis in obese adipose tissue, such that mmBCFAs are significantly decreased in obese animals. These results identify adipose tissue mmBCFA synthesis as a novel link between BCAA metabolism and lipogenesis, highlighting roles for CrAT and FASN promiscuity influencing acyl-chain diversity in the lipidome.

The branched-chain amino acids (BCAAs) leucine, isoleucine, and valine are essential amino acids important for protein synthesis, signaling, and bioenergetics. BCAA catabolism is emerging as a prominently dysregulated pathway in metabolic syndrome^{1,2} and cancer³; as such, a greater and more quantitative understanding of this pathway in mammalian physiology is needed. BCAA catabolism is initiated by deamination via branched-chain amino acid transferases (BCATs), and these branched-chain keto acids are subsequently metabolized in mitochondria to generate various acyl-CoA species downstream of the branched-chain keto-acid dehydrogenase (BCKDH) complex. This pathway is active in both energetically demanding tissues, such as heart and muscle, and lipogenic tissues⁴. Indeed, studies indicate that adipose BCAA catabolism can compensate for whole-body genetic deficiencies in the pathway⁵. Furthermore, carbon from leucine and isoleucine contribute significantly to de novo lipogenesis in differentiated adipocytes^{6,7}, suggesting that adipose tissue BCAA catabolism may be important for adipocyte function.

The predominant product of de novo lipogenesis in mammals is the saturated 16-carbon fatty acid (FA) palmitate, which is further elongated and/or desaturated in a tissue-specific manner. Both odd-chain (OCFAs) and monomethyl branched-chain FAs (mmBCFAs) are also present in mammals, but these species are considered to be predominantly diet derived outside of the skin^{8,9}. In lower organisms mmBCFAs are important for controlling membrane fluidity¹⁰ and contribute to neural development¹¹. In mammals, mmBCFAs are

found in milk¹², sebum¹³, and vernix¹⁴, and mmBCFA levels differ in obese and insulin-resistant patients^{15,16}. However, little is known about the metabolism of BCFAs in mammals. Here we demonstrate that mmBCFAs are endogenous products of fatty acid synthase (FASN) and that their in vivo synthesis is influenced by mitochondrial BCAA catabolism, tissue-specific expression of carnitine acetyltransferase (*Crat*), the microbiome, hypoxia, and diet. mmBCFAs are primarily synthesized in adipose depots and are decreased in the context of diet-induced obesity, in which adipose-specific hypoxia potently suppresses BCAA catabolism and lipogenesis. These results identify a metabolic pathway in mammals connecting BCAA metabolism and lipid biosynthesis to acyl-chain diversity that is coordinated across distinct tissues and potently regulated by hypoxia.

Results

Mammalian adipocytes synthesize mmBCFAs via FASN. Adipocytes undergo substantial mitochondrial and cytosolic metabolic reprogramming upon differentiation. We and others have previously shown that a distinct feature of this metabolic reprogramming is upregulation of BCAA catabolism, which becomes a substantial source of carbon for both TCA cycle metabolism and lipogenic acetyl-CoA^{6,7,17}. In cultured adipocytes, odd-chain FAs (C15:0 and C17:0) synthesized from valine- and isoleucine-derived propionyl-CoA can also accumulate as a result of vitamin B12 deficiency and decreased activity of the B12-dependent enzyme methylmalonyl-CoA mutase^{6,7}. In addition to the increased BCAA

¹Department of Bioengineering, University of California, San Diego, La Jolla, CA, USA. ²Departments of Chemistry, Molecular and Cell Biology, and Nutritional Science and Toxicology, University of California, Berkeley, Berkeley, CA, USA. ³Nomis Center for Immunobiology and Microbial Pathogenesis, The Salk Institute for Biological Studies, La Jolla, CA, USA. ⁴Division of Biological Sciences, University of California at San Diego, La Jolla, CA, USA.

⁵Division of Endocrinology, Division of Developmental Biology, Cincinnati Children's Hospital Research Foundation, Cincinnati, OH, USA. ⁶Department of Pediatrics, University of Cincinnati College of Medicine, Cincinnati, OH, USA. ⁷Division of Pediatric Endocrinology, Department of Pediatrics, University of California at San Diego, La Jolla, CA, USA. ⁸Virginia San Diego Healthcare System, San Diego, CA, USA. ⁹Division of Endocrinology & Metabolism, Department of Medicine, University of California at San Diego, La Jolla, CA, USA. ¹⁰Program in Molecular Medicine, University of Massachusetts Medical School, Worcester, MA, USA. ¹¹NAFLD Research Center, Division of Gastroenterology, Department of Medicine, University of California at San Diego, La Jolla, CA, USA. ¹²Moores Cancer Center, University of California, San Diego, La Jolla, CA, USA. ¹³Diabetes Research Center, University of California, San Diego, La Jolla, CA, USA. *e-mail: cmetallo@ucsd.edu

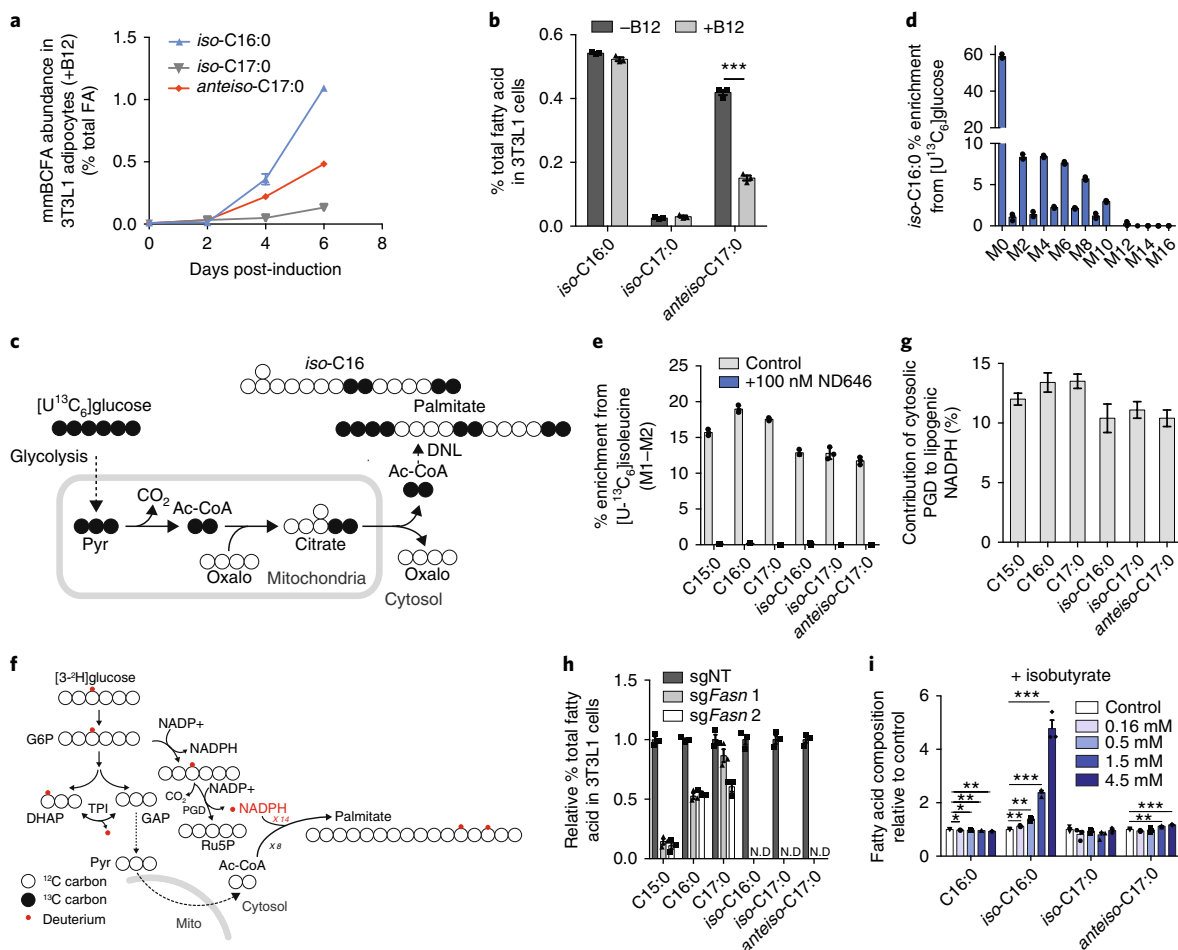


Fig. 1 | Mammalian adipocytes synthesize mmBCFAs via fatty acid synthase. a, mmBCFA abundance in differentiating 3T3L1 adipocytes. **b**), mmBCFA abundance in 3T3L1 adipocytes differentiated for 7 d with or without 500 nM B12. Two-tailed Student's *t*-test was performed on three cellular replicates ($P=0.000019$) with no adjustment for multiple comparisons. **c**, Atom-transition map demonstrating isotope incorporation into de novo synthesized fatty acids from $[U-^{13}C_6]$ glucose. Closed circles indicate ^{13}C carbon. DNL, de novo lipogenesis. **d**, Isotopologue distribution of *iso*-C16:0 from $[U-^{13}C_6]$ glucose-traced 3T3L1 cells. **e**, Percent enrichment from $[U-^{13}C_6]$ isoleucine-derived acetyl-CoA (M1–M2) only) in 3T3L1 adipocytes with or without 100 nM ND646 for 24 h. **f**, Atom-transition map depicting transfer of isotope $[3-^2H]$ glucose through glycolysis, the pentose phosphate pathway and reductive biosynthesis. Open circles indicate carbon and small red circles indicate a deuterium label from $[3-^2H]$ glucose. TPI, triose phosphate isomerase. **g**, Contribution of $[3-^2H]$ glucose-labeled NADPH to fatty acid de novo synthesis determined via ISA. 3T3L1 adipocytes cultured in tracer for 72 h. PGD, phosphogluconate dehydrogenase. **h**, *Iso*-C16:0 levels as percent total FA in pooled CRISPR–Cas9 FASN KO 3T3L1 adipocytes following addition of isobutyrate for 24 h. **i**, Relative abundances of mmBCFAs and C16:0 in differentiated 3T3L1s following addition of isobutyrate for 24 h. Two-tailed Student's *t*-test was performed on three cellular replicates for each comparison with no adjustment for multiple comparisons. All data are presented as means \pm s.e.m. with dot plots overlaid except for **g**, where 95% confidence intervals from ISA model are shown. All data are representative of three cellular replicates, and each experiment was repeated three independent times with the exception of **h**, for which two separate infections were carried out. The same result was obtained in each independent experiment. * $P < 0.05$, ** $P < 0.01$, *** $P < 0.001$.

catabolism and OCFA synthesis observed in differentiated 3T3L1 adipocytes, we detected accumulation of several mass isomers of the FAs C16:0 (palmitate) and C17:0 (heptadecanoate), which eluted before the predominant straight-chain isomers in our gas chromatography–mass spectrometry (GC–MS) analysis. As compromised B12 metabolism can lead to accumulation of monomethyl branched-chain FAs (mmBCFAs) in the brain¹⁸, we hypothesized that these alternate mass isomers were mmBCFAs and subsequently used analytical standards to confirm their identities. We detected increases in 14-methylpentadecanoate (*iso*-C16:0), 14-methylhexadecanoate (*anteiso*-C17:0) and 15-methylhexadecanoate (*iso*-C17:0) during differentiation of 3T3L1 adipocytes, with *iso*-C16:0 occurring at the highest abundance (Fig. 1a). These FAs have a single branch at either the penultimate or antepenultimate carbon of the acyl chain (Supplementary Fig. 1a), with the position impacting

elution times (Supplementary Table 1). Interestingly, the relative abundance of *anteiso*-C17:0 was impacted by B12 availability in this culture system (Fig. 1b), suggesting that these species were actively metabolized by adipocytes.

To determine whether mmBCFAs were synthesized de novo, we cultured 3T3L1 adipocytes with $[U-^{13}C_6]$ glucose, which generates ^{13}C fully labeled acetyl-CoA units and a distinct M+2 isotopologue pattern in newly synthesized FAs (Fig. 1c; Supplementary Fig. 1b). We detected significant enrichment in mmBCFAs (Fig. 1d; Supplementary Fig. 1c,d), demonstrating that these FAs are synthesized in a similar manner to palmitate, via acetyl-CoA incorporation. Additionally, treatment with the ACC inhibitor ND646 (ref. 19) led to a significant decrease in ^{13}C enrichment of both straight-chain FAs and mmBCFAs, indicating that their synthesis is dependent on malonyl-CoA from ACC (Fig. 1e).

Although cytosolic FASN is the predominant enzyme used for de novo lipogenesis in mammalian cells, mitochondrial FAS II has been proposed as a hypothetical route for mmBCFA synthesis in eukaryotes²⁰. To determine whether the cellular location of mmBCFA synthesis differed from that of palmitate, we traced adipocytes with [3-²H]glucose. Deuterium labeling on the third carbon of glucose specifically labels cytosolic NADPH via the oxidative pentose phosphate pathway but is lost in glycolysis and does not label citrate, acetyl-CoA or mitochondrial NADPH (Fig. 1f)²¹. If a significant portion of mmBCFAs were synthesized within mitochondria, decreased ²H enrichment relative to palmitate would be expected. We found that cytosolic NADPH effectively labeled both mmBCFAs and palmitate, suggesting that these FAs were primarily synthesized in the cytosol by FASN (Fig. 1g), albeit at slower rates than palmitate (Supplementary Fig. 1e,f). Next, we generated pooled cultures of 3T3L1 adipocytes with CRISPR-Cas9-mediated FASN knockout (KO) before differentiation (Supplementary Fig. 2a-b). Though the abundance of all FAs decreased, mmBCFAs were undetectable in all FASN KO cells and abundant in sgNT cells (Fig. 1h). However, differentiation was significantly impaired (Supplementary Fig. 2c). To further confirm that FASN deficiency rather than impaired differentiation and lack of substrate decreased BCFA synthesis, we supplemented cultures with the short branched-chain FAs isobutyrate, isovalerate, 2-methyl-butyrate, and propionate. Addition of these substrates increased the abundance of mmBCFA and OCFA in a dose-dependent manner (Fig. 1i; Supplementary Fig. 1d-f). Whereas *iso*-C16:0 levels significantly increased in control adipocytes and in nondifferentiated pre-adipocytes upon addition of isobutyrate, *iso*-C16:0 levels were still undetectable in FASN KO cells (Supplementary Fig. 2g), indicating that lack of FASN rather than impaired differentiation was the primary reason for the absence of BCFA synthesis. Furthermore, treatment with the FASN inhibitor TVB3166 significantly decreased the synthesis of both *iso*-C16:0 and palmitate (Supplementary Fig. 2h). Although the mitochondrial FAS II system may also contribute to mmBCFA synthesis, our results demonstrate that cytosolic de novo lipogenesis via FASN promiscuity is the primary driver of mmBCFA production in adipocytes²².

BCAA catabolic intermediates drive mmBCFA synthesis. The minor impact of B12 availability on *iso*-C16:0 and *iso*-C17:0 suggests that these FAs are not synthesized via elongation of methylmalonyl-CoA. Administration of radioisotopes in rats has indicated that BCAAs are precursors for mmBCFAs in skin²³. In addition, provision of isovaleryl-CoA, isobutyryl-CoA or 2-methylbutyryl-CoA to enzyme extracts from rat epididymal tissue results in the production of mmBCFAs²². To confirm that this pathway architecture exists within intact adipocytes, we cultured adipocytes with uniformly ¹³C-labeled BCAAs and quantified labeling via GC-MS. This resulted in distinct labeling patterns for each of their respective mmBCFAs (Fig. 2a-d). Carbon from [U-¹³C₅]valine was only incorporated into *iso*-C16:0 and resulted in a prominent M + 4 peak in the isotopologue distribution, indicating that the valine catabolic intermediate isobutyryl-CoA was used to synthesize *iso*-C16:0 (Fig. 2a,b). Similarly, *iso*-C17:0 from [U-¹³C₆]leucine and *anteiso*-C17:0 from [U-¹³C₆]isoleucine exhibited distinct M + 5 shifts, indicating that isovaleryl-CoA and 2-methylbutyryl-CoA were used for mmBCFA synthesis (Fig. 2a,c,d). Notably, we detected no FA isotopologues of M + 8 or M + 10, demonstrating that only a single incorporation of these branched intermediates into the acyl chain was occurring in these cells. This result, combined with the observation that only mmBCFAs with a branch at the penultimate or antepenultimate end were detected, supports a mechanism whereby FASN is promiscuous and can use short acyl-CoAs to initiate synthesis of long-chain FAs.

Multiple acyl-CoA dehydrogenases (ACAD) are annotated to carry out the dehydrogenations of isovaleryl-CoA, 2-methylbutyryl-CoA,

and isobutyryl-CoA. To evaluate the specific roles of these enzymes in BCAA catabolism and mmBCFA synthesis, we targeted various ACAD enzymes via shRNA-mediated knockdown and quantified FA abundances after adipocyte differentiation (Supplementary Fig. 3a-c). Knockdown of ACAD8, IVD and ACADSB specifically and significantly increased levels of *iso*-C16:0, *iso*-C17:0 and *anteiso*-C17:0, respectively (Fig. 2e-g; Supplementary Fig. 3d-f). Targeting of ACADM and ACADS did not impact mmBCFA levels appreciably. Each mmBCFA accumulated differently, with valine-derived *iso*-C16:0 having the highest abundance (Fig. 1a; Supplementary Fig. 3d), inversely consistent with the relative expression of each dehydrogenase (Fig. 2h). These findings indicate that ACAD enzyme expression influences the metabolic fate of BCAAs and mmBCFA production.

mmBCFAs are incorporated into distinct lipid species. The above data are representative of total hydrolyzed FA pools in the cell. To further characterize the metabolic fate of mmBCFAs, we next sought to determine whether mmBCFAs were incorporated into distinct lipid species. Distinguishing lipids containing different acyl chain isomers such as *iso*-C16:0 and C16:0 (palmitate) with liquid chromatography is challenging because of the decreased isomer resolution compared to gas chromatography, and there have been limited reports of mmBCFAs in specific, intact lipids^{11,24}. To circumvent this issue we used [U-¹³C₅]valine tracing to differentiate lipids containing C16:0 versus *iso*-C16:0 acyl-chains, as lipids synthesized with the latter would contain distinct M + 4 peaks (Supplementary Fig. 4a-c). We quantified M + 0 and M + 4 isotopologue abundances using targeted LC-MS/MS in 46 lipid species containing 16-carbon acyl chains in adipocytes cultured with [U-¹³C₅]valine or [¹²C]valine. Of those measured species, 11 lipids had significant enrichment of M + 4 ions in [U-¹³C₅]valine-traced cells over [¹²C]valine-traced cells (Supplementary Fig. 4d,e). The highest percent of total enrichments was observed in species containing alkyl chains, suggesting that *iso*-C16:0 may be selectively incorporated into ether lipids. Notably, some BCFA (for example, phytanic acid) must be trafficked to the peroxisome for α -oxidation, and peroxisomes are the site for ether lipid synthesis because of the presence of alkyl DHAP synthase and DHAPAT. As such, mmBCFAs may be similarly directed to the peroxisome, leading to the observed high enrichment in abundant alkyl-lipids. Other significantly enriched lipids included sphingomyelin, phosphatidylserine, phosphatidylcholine, phosphatidylinositol and triacylglycerols (TAGs). In fact, induction of lipolysis via isoproterenol treatment resulted in significant mmBCFA secretion into culture medium, indicating that these FAs are present in lipid droplets (Supplementary Fig. 4f).

mmBCFAs are de novo synthesized in vivo. To determine whether mmBCFA synthesis occurs in vivo, we quantified the abundances of each mmBCFA across various tissues in male and female C57BL/6J mice. Consistent with our observation of mmBCFA synthesis in adipocytes, white and brown adipose tissues (WAT and BAT) exhibited the highest abundances of all mmBCFAs, including *iso*-C18:0, an elongated derivative of *iso*-C16:0 that was not detectable in 3T3L1 cultures (Fig. 3a, b; Supplementary Fig. 5a,b). Liver and brain exhibited the lowest abundances of mmBCFAs, suggesting that FA composition is regulated in a tissue-specific manner. In addition, *iso*-C17:0 abundance differed between males and females, potentially because of hormonal effects on BCAA catabolism²⁵. With the exception of *anteiso*-C17:0, total mmBCFAs (free and lipid bound) were present in plasma at micromolar concentrations (Supplementary Fig. 5c), and their abundances increased 2-3 fold in plasma upon prolonged fasting (Fig. 3c; Supplementary Fig. 5d). Although these measurements are of total rather than free FAs, these data suggest that *iso*-BCFAs are released from adipose tissue via lipolysis along with other FAs.

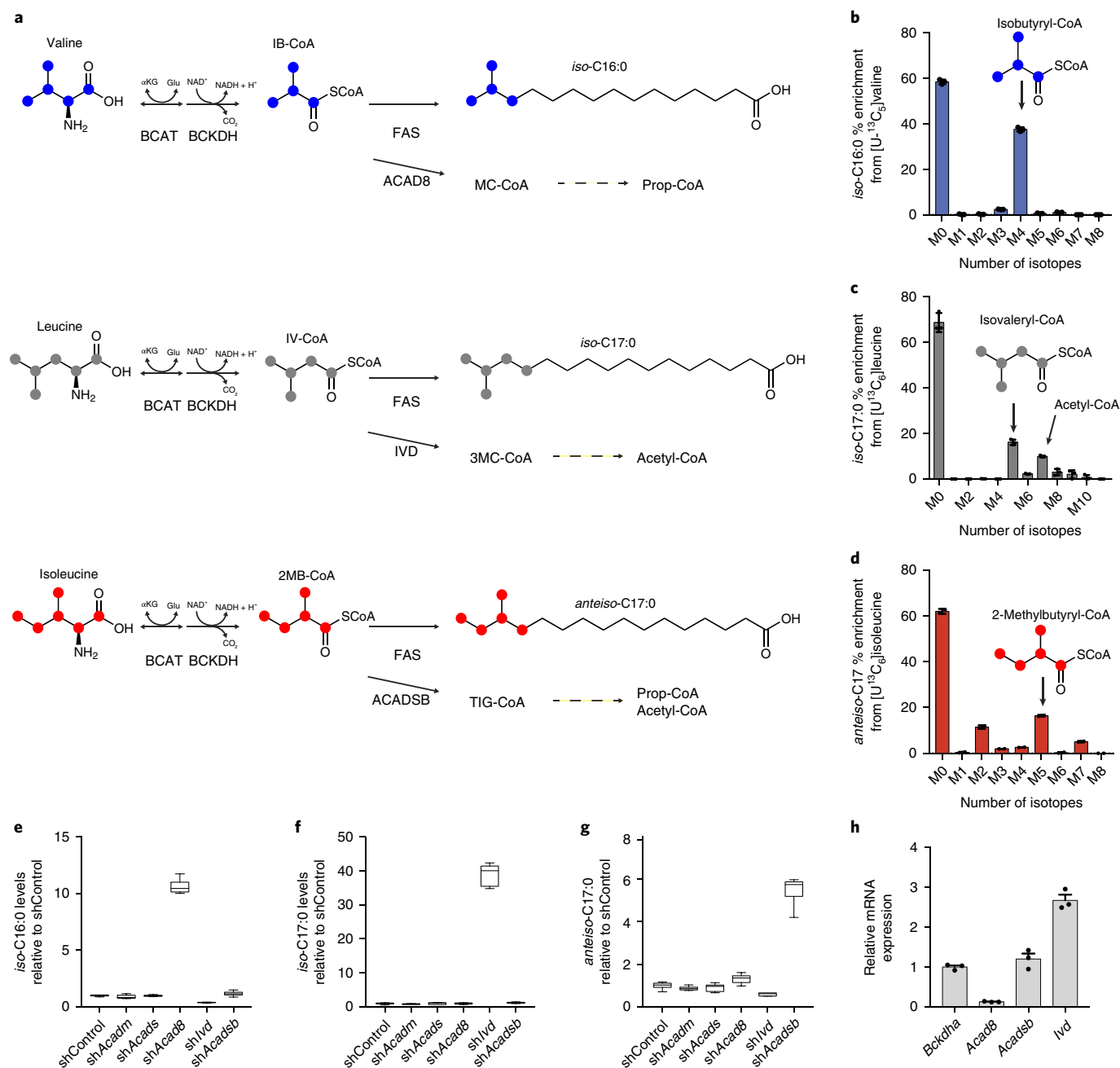


Fig. 2 | BCAA catabolic intermediates drive mmBCFA synthesis. **a**, Pathway depicting BCAA catabolism and mmBCFA synthesis. **b–d**, Isotopologue distributions of *iso*-C16:0 from [U-¹³C₆]valine (**b**) *iso*-C17:0 from [U-¹³C₆]leucine (**c**) and *anteiso*-C17:0 from [U-¹³C₆]isoleucine (**d**). Representative data from three cell replicates in **b–d**. **e–g**, Relative abundance of *iso*-C16:0 (**e**) *iso*-C17:0 (**f**) and *anteiso*-C17:0 (**g**) following knock down of ACAD enzymes. Representative data from six cell replicates are shown in **e–g**. **h**, Relative mRNA expression. Representative data are shown from three cell replicates. All experiments were carried out in 3T3L1 adipocytes. All experiments were repeated three independent times with similar results. Data are presented as means \pm s.e.m. with dot plots overlaid (**b–d**) or box (25th to 75th percentile with median line) and whiskers (min. to max. values) (**e–g**).

As microbial metabolism is a source of both long and short BCFA^{26,27} (Supplementary Fig. 6a), the gut microbiome could be a significant source of mmBCFAs in animals. In addition, mmBCFAs are present in chow (Supplementary Fig. 6b), and thus diet will also contribute to mmBCFA levels in vivo. To determine the relative contribution of de novo synthesis versus diet and the impact of microbiota on mmBCFA levels, we administered ²H₂O to germ-free and specific pathogen-free (SPF) control mice for 8 d and measured enrichment of FAs in lipogenic tissues²⁸ (Fig. 3d). A significant fraction of the mmBCFAs present were newly synthesized in both germ free and SPF mice

(Fig. 3e, f; Supplementary Fig. 6c,d). Valine-derived *iso*-C16:0 was the most abundantly synthesized mmBCFA (Fig. 3g, h; Supplementary Fig. 6e,f), and the fraction of newly synthesized *iso*-C16:0 was similar to that for palmitate (C16:0) in eWAT, iWAT and BAT (Fig. 3e, f; Supplementary Fig. 6c). Overall, these data indicate that de novo synthesis is a significant source of mmBCFAs in vivo, and their production can occur in the absence of microbiota. However, both levels (Supplementary Fig. 6g–j) and synthesis of mmBCFAs and other FAs differed significantly in the adipose tissues of germ-free and SPF mice, indicating that microbiota impacts lipogenesis and FA diversity.

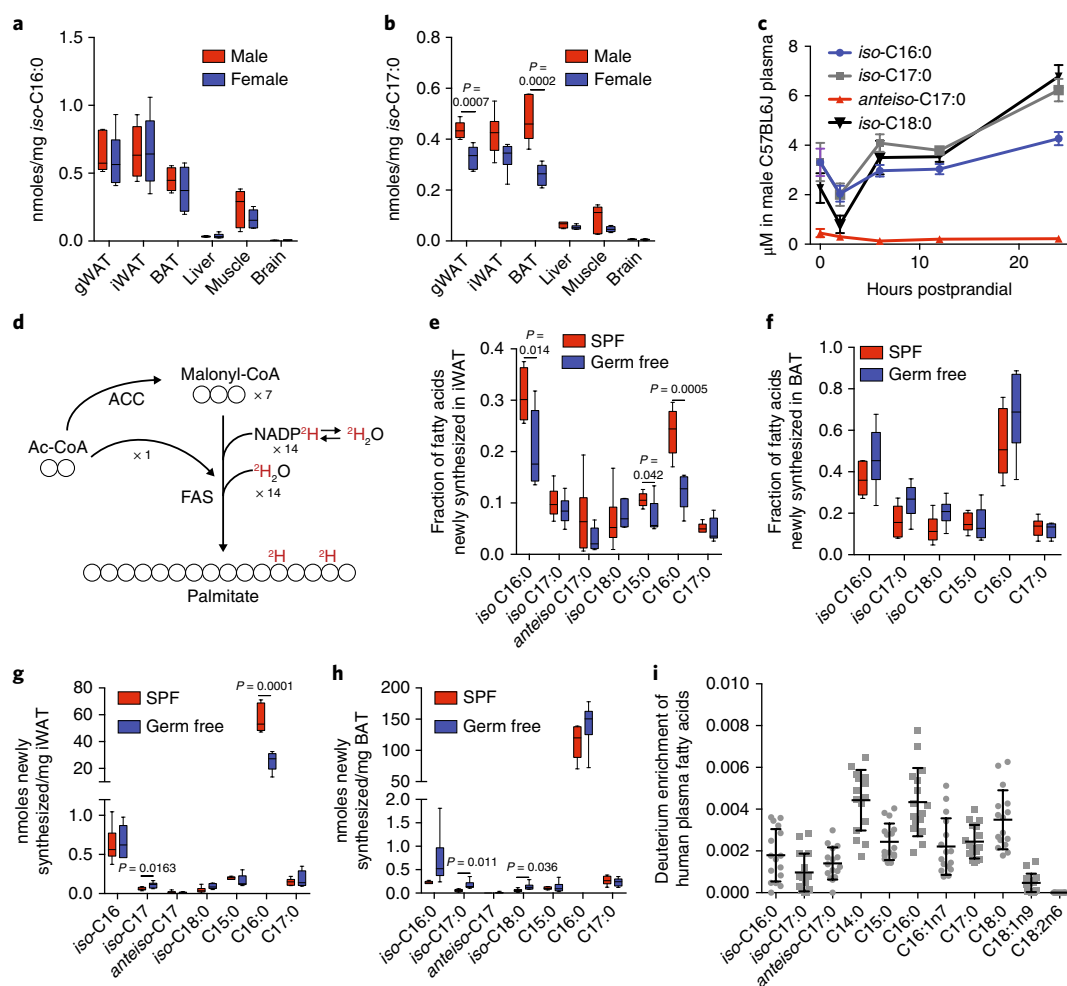


Fig. 3 | mmBCFAs are de novo synthesized in vivo. **a,b**, Abundance of *iso*-C16:0 (**a**) and *iso*-C17:0 (**b**) in various tissues from C57BL/6J male ($n=6$) and female mice ($n=6$). **c**, Plasma concentration of total hydrolyzed mmBCFAs from C57BL/6J male mice ($n=8$) following removal of food at time 0 (7 a.m.), sampled at 2 h, 6 h, 12 h and 24 h. **d**, Incorporation of $^2\text{H}_2\text{O}$ into newly synthesized fatty acids. **e,f**, Fractional synthesis of fatty acids in iWAT (**e**) and BAT (**f**) of germ-free ($n=6$) and SPF mice ($n=6$). **g,h**, Amount of newly synthesized fatty acids present in iWAT (**g**) and BAT (**h**) of germ-free ($n=6$) and SPF mice ($n=6$). **i**, Deuterium enrichment of plasma FAs in NAFLD patients ($n=16$) normalized to the area under the curve of plasma $^2\text{H}_2\text{O}$ levels from day 0 to day 21 for each patient. Two-tailed Student's *t*-test was performed for each comparison in this figure with no adjustment for multiple comparisons. Data are presented as means \pm s.e.m. (**c**), means \pm s.d. with dot plots overlaid (**i**), or box (25th to 75th percentile with median line) and whiskers (min. to max. values) (**a,b,e-h**).

To confirm that de novo synthesis of mmBCFAs occurs in humans, we analyzed plasma from NAFLD patients who were administered $^2\text{H}_2\text{O}$ (Supplementary Table 2 and Supplementary Fig. 6k,l). Analysis of deuterium enrichment of FAs demonstrated that both OCFAs and mmBCFAs were synthesized de novo in humans (Fig. 3i). Plasma mmBCFAs were present in the range of 1–20 μM in these patients (Supplementary Fig. 6m), comparable to those of other long and very long chain FAs such as C20:0 and C24:0 (ref. 29).

BCAA flux to mmBCFAs is decreased by diet-induced obesity.

Clinical studies have indicated that BCAA metabolism is dysregulated in the context of metabolic syndrome, as plasma BCAAs and some catabolites are elevated in insulin-resistant patients¹². Additionally, BCAA catabolic enzyme expression is decreased in rodents fed a high-fat diet (HFD)¹⁷. Conversely, plasma mmBCFAs are decreased in morbidly obese patients¹⁵. To determine whether mmBCFA levels change in mouse models of obesity, we quantified total FAs in plasma and WAT of mice fed a HFD or low-fat diet (LFD) for 15 weeks. Although intake of all FAs (including

mmBCFAs) was increased in the HFD cohort (Supplementary Fig. 7a), *iso*-BCFA abundances were significantly lower (Fig. 4a,b; Supplementary Fig. 7b-c). In terms of fold changes, valine-derived *iso*-C16:0 and *iso*-C18:0 were the most differentially abundant FAs in these tissues. Relative abundances of straight-chain FAs increased or remained unchanged, with the exceptions of C16:1 (palmitoleate) and C15:0 (Fig. 4a). Similar results were observed in ob/ob mice, in which mmBCFAs were significantly decreased in iWAT relative to control mice (Supplementary Fig. 7d). Notably, *anteiso*-C17:0 levels increase in the plasma of HFD mice (Fig. 4b). Given that synthesis of *anteiso*-C17:0 was nearly undetectable in $^2\text{H}_2\text{O}$ traced mice (Fig. 3g,h), this FA is primarily diet derived and synthesis from isoleucine is not significant in vivo. These results demonstrate that individual FAs change distinctly with the onset of obesity depending on their origin and metabolism.

To directly investigate altered BCAA catabolism in the context of metabolic syndrome, we fed C57BL/6J mice a HFD or LFD for 12 weeks and then identical diets formulated with 25% enriched [$^{13}\text{C}_5$, ^{15}N]valine and [$^{13}\text{C}_6$, ^{15}N]leucine for 3 weeks (Supplementary Fig. 8a). Although fasting plasma glucose levels

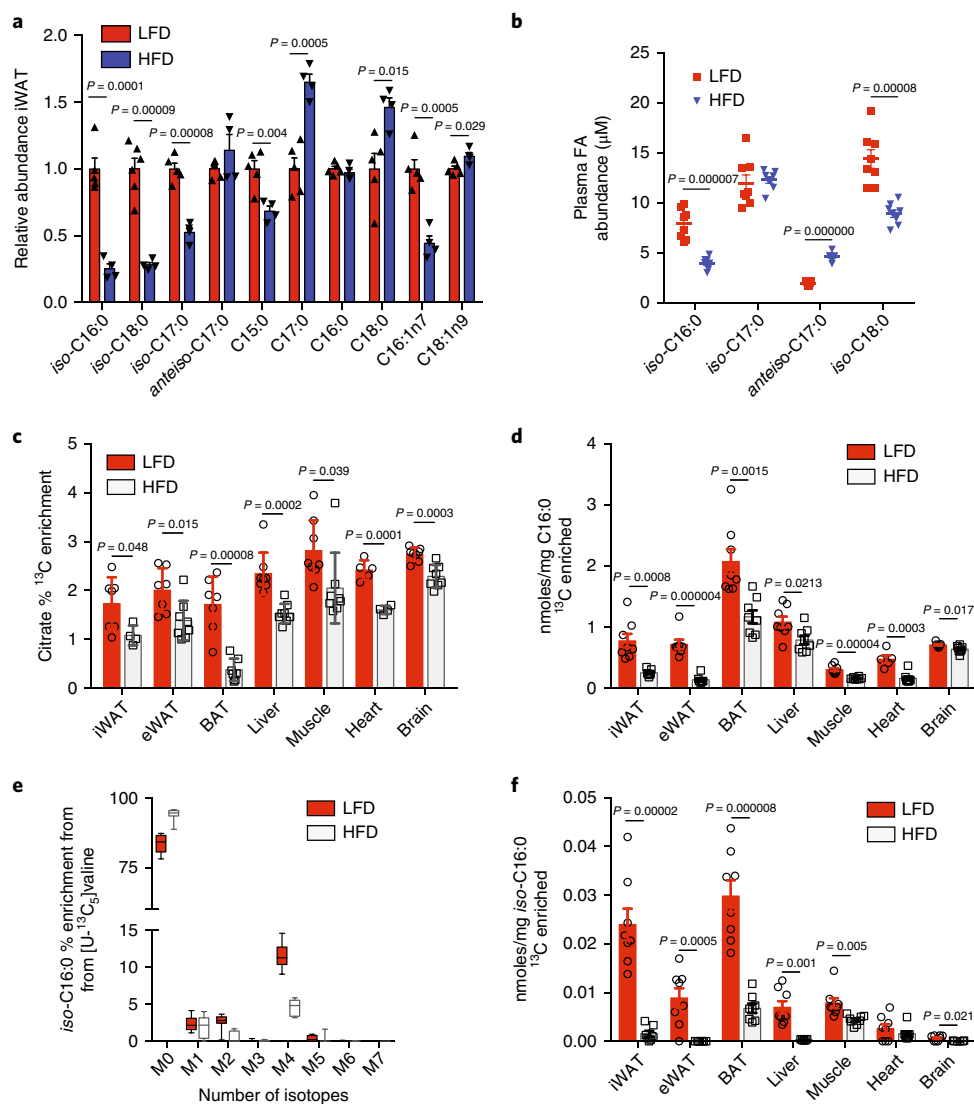


Fig. 4 | BCAA flux to mmBCFAs is decreased by diet-induced obesity. **a**, Relative abundances of FAs in iWAT from C57BL/6 J mice fed a HFD ($n = 4$) or a LFD ($n = 5$) for 15 weeks. **b**, Total FA abundances in plasma from C57BL/6 J mice fed a HFD ($n = 8$) or a LFD ($n = 8$) for 15 weeks. **c–f**, ^{13}C enrichment in specified metabolites from HFD or LFD fed mice with 25% of valine and leucine supplied as $[\text{U}^{13}\text{C}, ^{15}\text{N}]$ isotope. **(c)**, Citrate percent ^{13}C enrichment. $N = 8$ for all comparisons except LFD iWAT ($n = 7$), eWAT ($n = 7$), BAT ($n = 7$) and HFD iWAT ($n = 4$), BAT ($n = 7$), heart ($n = 4$). **d**, ^{13}C molar enrichment of C16:0. $N = 8$ for all comparisons except LFD eWAT ($n = 7$), heart ($n = 5$) and HFD iWAT ($n = 7$). **e**, Isotopologue distribution of *iso*-C16:0 from $[\text{U}^{13}\text{C}_5]$ valine (HFD, $n = 8$; LFD, $n = 8$). **f**, ^{13}C molar enrichment of *iso*-C16:0. $N = 8$ for all comparisons except HFD iWAT ($n = 7$), liver ($n = 5$) and brain ($n = 6$). Two-tailed Student's *t*-test was performed for each comparison in this figure with no adjustment for multiple comparisons. Data are presented as means \pm s.e.m. with dot plot overlaid (**a–d, f**) or box (25th to 75th percentile with median line) and whiskers (min. to max. values) (**e**).

were elevated (Supplementary Fig. 8b), plasma BCAA levels were unchanged (Supplementary Fig. 8c), consistent with recent studies in C57BL/6J mice³⁰, and we observed no differences in enrichment of plasma leucine and valine (Supplementary Fig. 8d). However, significant differences were present within tissues (Supplementary Fig. 8e,f). We detected significant ^{13}C enrichment of citrate and palmitate in all tissues measured (Fig. 4c,d), indicating that leucine catabolism is a significant source of acetyl-CoA in vivo. In the HFD cohort, ^{13}C enrichment and molar abundance in citrate and palmitate, respectively, were significantly decreased in all tissues, with BAT being the most impacted, demonstrating that diet-induced obesity decreases BCAA catabolism (Fig. 4c,d). The leucine and valine-derived mmBCFAs had characteristic mass shifts of M + 4 and M + 5, indicating that these FAs were synthesized de novo from BCAAs in vivo (Fig. 4e; Supplementary Fig. 8g,h). Importantly, molar enrichment of *iso*-BCFAs from valine and leucine were

decreased in total FA pools from almost all tissues analyzed (Fig. 4f; Supplementary Fig. 8i,j). The highest abundances of newly synthesized, long-chain *iso*-BCFAs were present in BAT, although cross-tissue transport is likely significant given the high FA enrichments detected in muscle and heart. Collectively, these data indicate that diet-induced obesity significantly decreases BCAA catabolic flux, and a downstream result of this regulation is lower mmBCFA synthesis and abundance throughout the body.

In contrast to mmBCFAs, we did not detect a pronounced M + 3 shift in OCFAs (Supplementary Fig. 8k), consistent with the abundance of other propionate sources in animals (for example, gut microbes, OCFAs oxidation, and cholesterol breakdown) or their production via α -oxidation³¹. Although valine is a source of propionate in cultured adipocytes, this pathway is not a major source of OCFAs in vivo under normal physiological conditions^{6,7}. However, we did note some incorporation of BCAA-derived carbon into

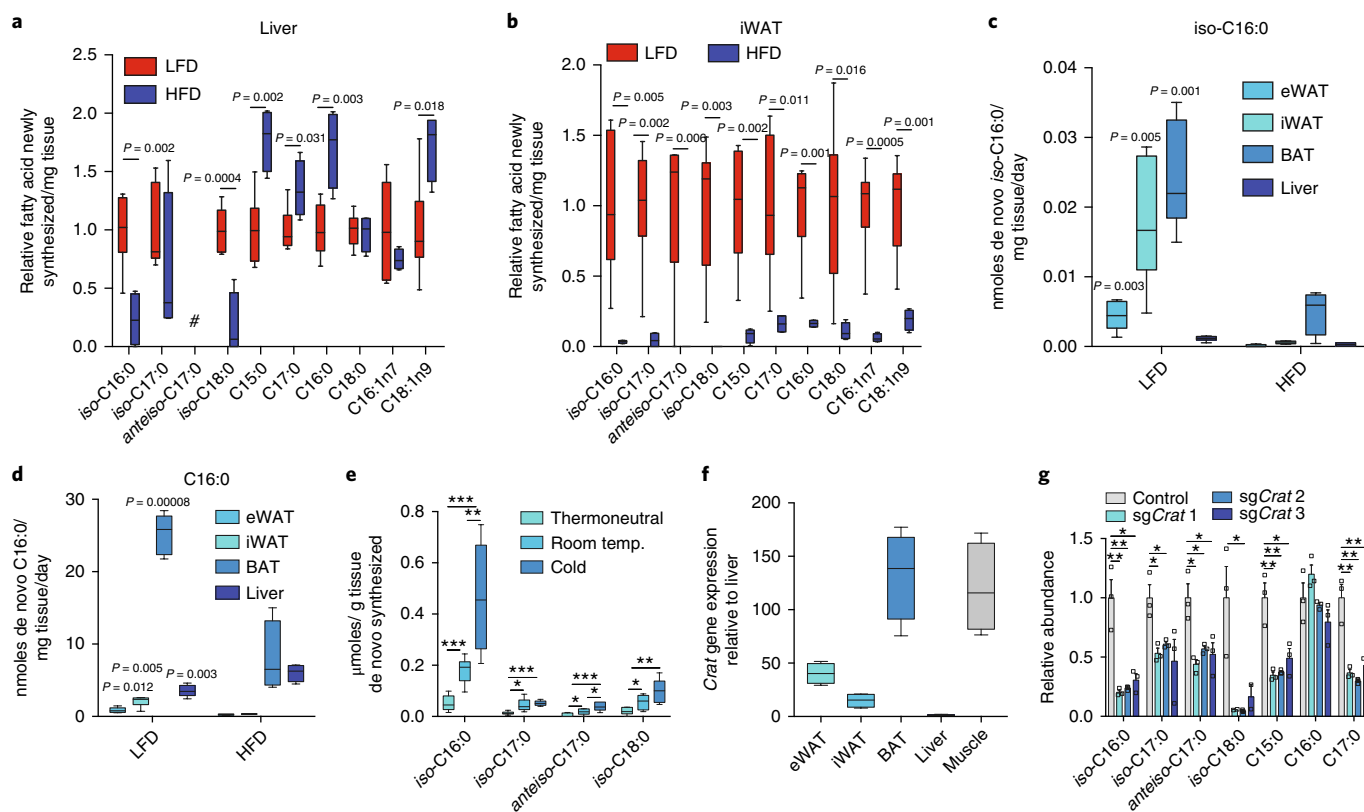


Fig. 5 | Adipose tissue mmBCFA synthesis is facilitated by CrAT. **a, b**, Fold difference in the levels of newly synthesized FAs present in liver (**a**) and iWAT (**b**). LFD ($n = 6$) and HFD ($n = 4$) were compared in **a** and **b**. **c**, De novo lipogenic turnover of iso-C16:0 across the primary lipogenic tissues. **d**, De novo lipogenic turnover of C16:0 across the primary lipogenic tissues. LFD ($n = 6$) and HFD ($n = 4$) for all comparisons. P values indicate intra-tissue comparison between HFD and LFD. **e**, Amount of newly synthesized FAs in BAT of mice exposed to thermoneutral (30 °C), room temperature (22 °C), or acclimatized to severe cold (6 °C) over 1 month ($n = 6$ per group). **f**, *Crat* expression relative to liver in tissues from male C57BL/6J mice ($n = 4$). **g**, Relative abundance of total FAs in pooled CRISPR–Cas9 *Crat* KO 3T3L1 adipocytes. Representative data from three cell replicates. Three independent infections have been carried out with the same result. Data is presented as box (25th to 75th percentile with median line) and whiskers (min. to max. values) (**a–f**) or means \pm s.e.m. with dot plots overlaid (**g**). Two-tailed Student's *t*-test was performed for each comparison in this figure with no adjustment for multiple comparisons. * $P < 0.05$, ** $P < 0.01$, *** $P < 0.001$.

OCFAs via acetyl-CoA (Supplementary Fig. 8l,m), indicating that OCFAs are also de novo synthesized to some extent in vivo.

Adipose tissue mmBCFA synthesis is facilitated by CrAT. The above results demonstrate that BCAA catabolic flux contributes significantly to de novo lipogenesis in vivo, and mmBCFAs are abundant products of this pathway. The large (~10-fold) differences in abundance within liver and adipose tissues (Fig. 3a,b) suggest that mmBCFA synthesis is regulated distinctly in these tissues. To assess the impact of diet on tissue-specific mmBCFA synthesis and enable a comparison to synthesis of other FAs, we administered $^2\text{H}_2\text{O}$ to HFD and LFD mice and measured enrichment in lipogenic tissues. Newly synthesized iso-C16:0 and iso-C18:0 were decreased in livers of HFD mice more than any other FA in terms of fold-change (Fig. 5a). In contrast, straight-chain and monounsaturated FA synthesis in the liver was increased or remained the same (Fig. 5a; Supplementary Fig. 9a). Within adipose tissues, HFD feeding decreased lipogenesis of all FAs, indicating that pathway activity is generally suppressed (Fig. 5b; Supplementary Fig. 9b–d) as previously observed^{32,33}. We next estimated FA synthesis and turnover occurring in each tissue on the basis of the molar abundance of each FA, fraction synthesized, and length of time the tracer was administered. mmBCFA turnover was highest in white and brown adipose tissues but substantially lower in liver (Fig. 5c; Supplementary Fig. 9e–g). Though brown adipose tissue

exhibited the highest synthesis and turnover for all FAs, these measurements are likely a lower estimate because they do not account for β -oxidation and futile FA cycling, which are likely quite high in brown adipocytes³⁴. HFD suppressed the synthesis of all FAs in adipose tissues but increased palmitate synthesis and turnover in liver (Fig. 5d). These results suggest that subcutaneous and brown adipocytes exhibit a high capacity for mmBCFA synthesis when lipogenesis is active in these depots. Indeed, mmBCFA synthesis in brown adipose tissue is significantly increased in cold-exposed mice (Fig. 5e), similar to the increased de novo lipogenesis of other FAs³⁴.

Liver exhibited relatively low abundances of newly synthesized mmBCFAs compared to other lipogenic tissues, and these levels decreased further in response to HFD, which contrasts to the changes observed for other FAs in the liver. Importantly, this tracing method does not account for lipid efflux and intertissue FA transport, and thus likely underestimates absolute FA synthesis in liver. Nevertheless, our collective data on abundance and synthesis of all FAs strongly indicate that mmBCFAs are synthesized in adipose tissues but not liver.

BCAA catabolism and lipogenesis are highly active in liver, so we next attempted to address why mmBCFA synthesis is specific to adipose tissues. mmBCFA synthesis requires BCAA catabolic intermediates to be exported from the mitochondria into the cytosol for elongation by FASN. Prior studies have demonstrated that CrAT, but not carnitine palmitoyltransferase 2 (CPT2), exhibits

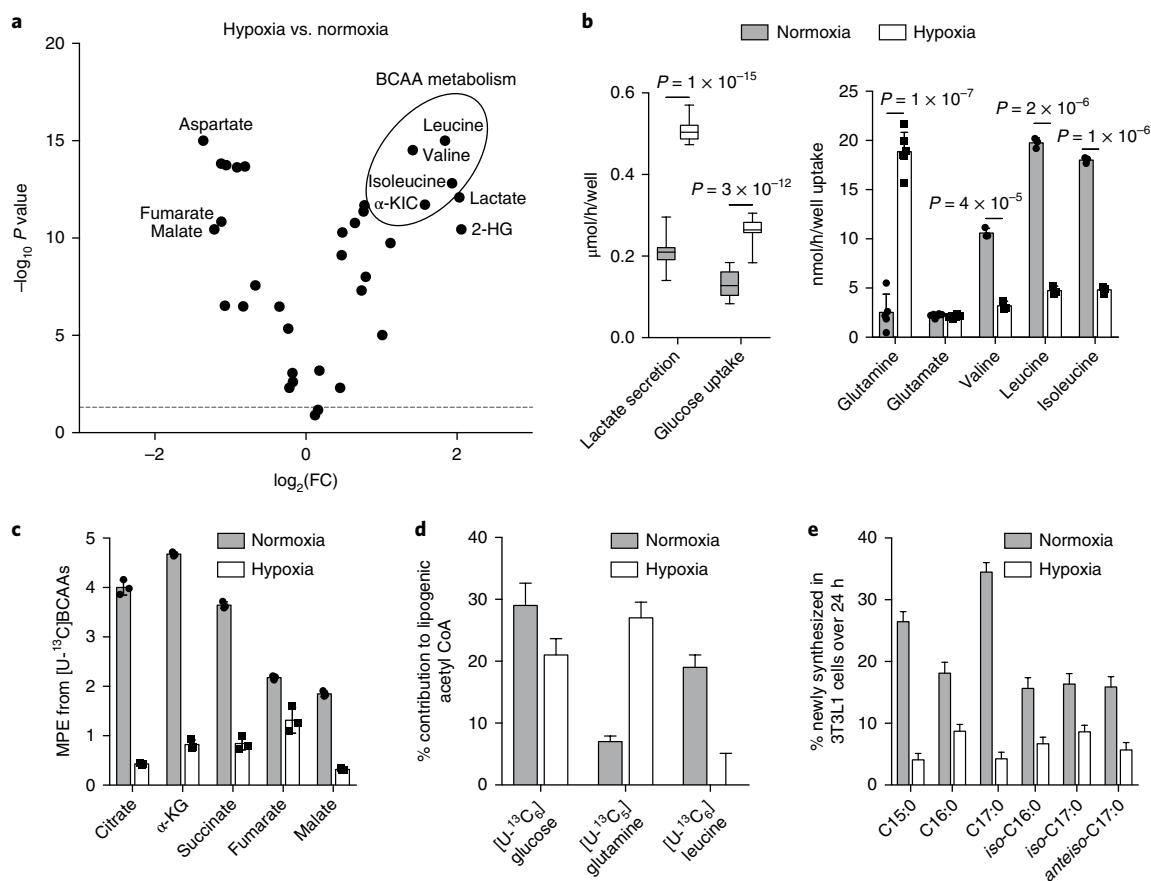


Fig. 6 | Hypoxia suppresses BCAA catabolism and mmBCFA synthesis in adipocytes. **a**, Volcano plot of changes in metabolite abundance in 3T3L1 cells exposed to hypoxia (1% O_2) or normoxia for 48 h. 12 cell replicates. **b**, Glucose and amino acid uptake by 3T3L1 cells in hypoxia (1%) or normoxia. 14 cell replicates for lactate and glucose; 6 cell replicates for glutamine and glutamate; 3 cell replicates for leucine, isoleucine and valine. Two-tailed Student's *t*-test was performed for each comparison in **a** and **b** with no adjustment for multiple comparisons. **c**, Mole percent enrichment (MPE) of TCA intermediates from $[U-^{13}\text{C}]$ BCAAs in 3T3L1s following 24 h of tracing in hypoxia (1%) or normoxia. **d**, Relative contribution of different substrates to lipogenic acetyl-CoA in 3T3L1s as determined by ISA following 24 h of tracing in hypoxia (1%) or normoxia. **e**, Percent of each FA newly synthesized over 24 h in hypoxia (1%) or normoxia. Three cell replicates are shown in **c–e**. All experiments were repeated three independent times with the same results. Data are presented as means \pm s.e.m. with dot plots overlaid, with exception of **b**, in which data is presented as box (25th to 75th percentile with median line) and whiskers (min. to max. values), and **d,e** as mean \pm 95% confidence interval.

enzyme activity toward BCAA-derived, short branched-chain CoAs³⁵. Therefore, we hypothesized that CrAT facilitates mmBCFA synthesis in adipose tissues. *Crat* mRNA is expressed at low levels in liver but exhibits high expression in muscle and adipose tissues (Fig. 5f). Additionally, quantitative proteomics indicates that CrAT is expressed at higher levels in white and brown adipose tissue compared to liver and brain (Supplementary Fig. 10a)³⁶. Thus, tissue-specific CrAT expression may be a driver of the observed differences in mmBCFA abundance and synthesis between liver, brain, and adipose tissues.

To more directly determine how CrAT influences mmBCFA synthesis, we generated CrAT KO 3T3L1 cells using CRISPR–Cas9 (Supplementary Fig. 10b). In contrast to the results with FASN KO, CrAT KO did not appreciably impact adipogenesis (Supplementary Fig. 10c,d). However, CrAT KO adipocytes had significantly decreased levels of both mmBCFAs and OCFAs (Fig. 5g), with minimal differences in the levels of other FAs (Supplementary Fig. 10e). These data indicate that CrAT is an important component of the mmBCFA synthesis pathway, facilitating cytosolic export of precursor acyl-CoAs (Supplementary Fig. 10f). Differential expression of this enzyme in liver versus BAT and WAT likely contributes to the tissue specificity of mmBCFA synthesis and abundance.

Hypoxia suppresses BCAA catabolism and mmBCFA synthesis.

Our data indicate that mmBCFAs are predominantly synthesized in adipose depots, and they decrease in the context of diet-induced obesity and increase in plasma during prolonged fasting. Given the adipose origin of mmBCFAs, we sought to determine the physiological factors that drive decreased BCAA catabolism and mmBCFA synthesis in obesity in vivo. Hypoxia has been proposed as a key contributory factor to adipose tissue dysfunction in obesity³⁷, and increasing adipose vascularization improves insulin sensitivity³⁸. To test the impact of hypoxia on BCAA metabolism in adipocytes, we incubated differentiated 3T3L1 adipocytes in 1% oxygen for 24 h before switching to hypoxia-equilibrated media containing uniformly ^{13}C -labeled amino acids or glucose for an additional 24 h. Intracellular BCAAs and α -ketoisocaproate accumulated significantly in hypoxic cultures along with lactate and 2-hydroxyglutarate (Fig. 6a). Media analysis demonstrated that glycolytic flux increased along with net glutamine consumption, whereas BCAA uptake decreased approximately 3–4 fold (Fig. 6b). Consistent with these flux changes, TCA intermediate enrichment from $[U-^{13}\text{C}]$ BCAAs was decreased under hypoxia (Fig. 6c). Isotopomer spectral analysis (ISA) demonstrated that the relative contribution of leucine to lipogenic acetyl-CoA decreased significantly, whereas the contribution

of glutamine to FAs increased (Fig. 6d). Notably, hypoxia generally decreased the synthesis of FAs, including OCFAs and mmBCFAs (Fig. 6e). Collectively, these data indicate that hypoxia strongly decreases BCAA catabolism. These results were recapitulated in primary cells derived from various tissues, including murine brown adipocytes, human skeletal myotubes, and white adipocytes (Supplementary Fig. 11a).

Bckdha and *Bcat2* mRNA and protein product were decreased under hypoxia in 3T3L1 adipocytes (Supplementary Fig. 11b–d). Additionally, we observed that adipose tissue oxygen tension and arterial blood flow were specifically decreased in HFD mice along with BCKDHA protein levels (Supplementary Fig. 11e–g), corroborating previous findings in obese adipose tissue^{17,39}. Overall, these data indicate that adipose tissue in obese animals exhibits lower oxygen tension, which may contribute to the observed decreases in BCAA catabolism and the BCKDHA levels we observed in adipose tissue from HFD mice. In turn, decreased flux through this pathway decreases local and circulating *iso*-mmBCFA levels in obesity.

Discussion

Here, using *in vitro* and *in vivo* metabolic tracing, we define a cross-tissue metabolic pathway in which BCAA catabolic flux and the promiscuity of FASN and CrAT within brown and white adipose tissues support mmBCFA synthesis. Additionally, we demonstrate that mmBCFA turnover is suppressed by HFD and obesity-induced adipose hypoxia. Collectively, these results demonstrate that mmBCFAs are endogenous FAs produced by adipocytes that link mitochondrial BCAA catabolism, lipogenesis, and diet to metabolic disease.

To date, the primary metabolic role of BCAA catabolism has been attributed to its importance as a nitrogen donor⁴⁰, to the production of HIBA to modulate FA uptake⁴¹, and to the generation of branched acyl intermediates that can modulate enzyme function via post-translational modifications⁴². Our data add to this knowledge, linking BCAA catabolism to modulation of FA diversity via enzyme promiscuity. Interestingly, mmBCFAs are synthesized and present at low levels in liver despite the high abundance of BCKDH and rate of lipogenesis^{43,44}. We provide evidence that this difference is driven by differential expression of *Crat*, encoding an enzyme that has predominantly been studied in muscle, where it is thought to mitigate fatigue by facilitating acetyl-CoA consumption during exercise and preventing acetyl-CoA accumulation during rest⁴⁵, thus decreasing macronutrient-induced lysine acetylation of mitochondrial proteins⁴⁶. However, its relevance in brown and white adipose tissues has not been explored, despite the high level of expression observed in brown adipose tissue³⁶. Given recent evidence that branched acyl-lysine modifications also alter mitochondrial enzyme function⁴², it is possible that diversion of branched CoA intermediates to long-chain FAs via CrAT is beneficial for maintaining healthy mitochondrial function.

We also highlight an underappreciated aspect of *de novo* lipogenesis, whereby the *de novo* FA composition reflects the balance of acyl-CoAs within the body. Thus, FASN promiscuity integrates changes in amino acid metabolism and short-chain FAs into the lipidome. Therefore, alterations in SCFA and acyl-CoA abundance driven by the gut microbiome, diet, or inborn errors of metabolism can influence FA diversity and must be considered when studying the pathophysiology of associated diseases. Indeed, elevated levels of mmBCFAs have been detected in the brains of patients with defects in cobalamin metabolism¹⁸. Supraphysiological levels of mmBCFAs could impact neuronal function and play a role in the neurological defects that occur in patients with certain organic acidemias or B12 deficiency. This work also highlights the limited resolution of most lipidomics platforms for resolving mmBCFA-containing lipids. We found that mmBCFAs are incorporated into diverse lipid species by cultured adipocytes, including ether lipids, TAGs, and phospholipids.

However, more extensive and focused approaches are needed to fully characterize their fates within different tissues.

Using ¹³C-labeled leucine and valine chow, we observed that HFD feeding suppressed BCAA catabolism, resulting in decreased mmBCFA synthesis. This result is consistent with transcriptional and other flux-based measurements that indicate downregulation of this pathway in mouse models of obesity and in diabetic patients^{17,47}. In fact, mmBCFAs correlate negatively with metabolic disease biomarkers such as C-reactive protein and insulin resistance in patients^{15,16}. This contrasts with levels of BCAAs and their downstream catabolic intermediates, which increase in the plasma of insulin-resistant patients^{14,41}. However, BCAA levels did not increase in our model of diet-induced obesity, and thus mmBCFA levels did not correlate with BCAA levels as might be expected. This is presumably due to the adipose-specific origin of these FAs, as BCAAs are widely catabolized in energetically demanding tissues such as muscle, liver, heart and brain, which are not significant sources of mmBCFAs. Furthermore, turnover and abundance of BCAA is much greater than that of mmBCFA. Therefore, although mmBCFA synthesis is impacted by BCAA catabolic flux, differential mmBCFA production is unlikely to be a primary driver of BCAA accumulation in T2D patients. Nevertheless, mmBCFAs may be a strong biomarker of adipose tissue lipogenesis and BCAA catabolism, and, in contrast to circulating BCAA levels, are not overtly influenced by changes in protein turnover and muscle insulin resistance.

The functional consequences of decreased mmBCFA levels are unknown. Despite their abundance in tissues and presence at micromolar levels in plasma, mmBCFAs have been studied minimally in the context of mammalian biology. mmBCFA-containing lipids play critical roles in the postembryonic growth, neuronal development and the foraging behavior of *C. elegans*^{11,48}. In prokaryotes BCFAs influence membrane fluidity, and their abundances change in response to certain stresses^{10,26}. In mammalian biology, previous studies have suggested they influence colon epithelial cell inflammation⁴⁹ and protect against necrotizing enterocolitis⁵⁰. Our insights into the metabolic origins and fates of mmBCFAs suggest other potential functions. As mmBCFAs are primarily synthesized in adipose tissue, incorporated into TAGs, and increase in plasma during fasting, these lipids may be involved in nutrient sensing and signal to other tissues in the body. However, given the relatively low abundance of mmBCFAs, these FAs are unlikely to contribute significantly to energy storage or substrate oxidation and are more likely to play a role in signaling or membrane structure. Ultimately, understanding the factors that regulate mmBCFA physiology is an essential step in elucidating their function and contribution to the biological importance of the BCAA catabolic pathway.

Online content

Any methods, additional references, Nature Research reporting summaries, source data, statements of data availability and associated accession codes are available at <https://doi.org/10.1038/s41589-018-0132-2>.

Received: 19 December 2017; Accepted: 2 August 2018;

Published online: 16 October 2018

References

1. Newgard, C. B. et al. A branched-chain amino acid-related metabolic signature that differentiates obese and lean humans and contributes to insulin resistance. *Cell Metab.* **9**, 311–326 (2009).
2. Wang, T. J. et al. Metabolite profiles and the risk of developing diabetes. *Nat. Med.* **17**, 448–453 (2011).
3. Tönjes, M. et al. BCAT1 promotes cell proliferation through amino acid catabolism in gliomas carrying wild-type IDH1. *Nat. Med.* **19**, 901–908 (2013).

4. Overmyer, K. A. et al. Maximal oxidative capacity during exercise is associated with skeletal muscle fuel selection and dynamic changes in mitochondrial protein acetylation. *Cell Metab.* **21**, 468–478 (2015).
5. Herman, M. A., She, P., Peroni, O. D., Lynch, C. J. & Kahn, B. B. Adipose tissue branched chain amino acid (BCAA) metabolism modulates circulating BCAA levels. *J. Biol. Chem.* **285**, 11348–11356 (2010).
6. Crown, S. B., Marze, N. & Antoniewicz, M. R. Catabolism of branched chain amino acids contributes significantly to synthesis of odd-chain and even-chain fatty acids in 3T3-L1 adipocytes. *PLoS ONE*, **10**, e0145850 (2015).
7. Green, C. R. et al. Branched-chain amino acid catabolism fuels adipocyte differentiation and lipogenesis. *Nat. Chem. Biol.* **12**, 15–21 (2016).
8. Ran-Ressler, R. R., Bae, S., Lawrence, P., Wang, D. H. & Brenna, J. T. Branched-chain fatty acid content of foods and estimated intake in the USA. *Br. J. Nutr.* **112**, 565–572 (2014).
9. Jenkins, B., West, J. A. & Koulman, A. A review of odd-chain fatty acid metabolism and the role of pentadecanoic Acid (c15:0) and heptadecanoic Acid (c17:0) in health and disease. *Molecules* **20**, 2425–2444 (2015).
10. Mercier, R., Domínguez-Cuevas, P. & Errington, J. Crucial role for membrane fluidity in proliferation of primitive cells. *Cell Rep.* **1**, 417–423 (2012).
11. Kniazeva, M., Zhu, H., Sewell, A. K. & Han, M. A lipid-TORC1 pathway promotes neuronal development and foraging behavior under both fed and fasted conditions in *C. elegans*. *Dev. Cell* **33**, 260–271 (2015).
12. Gibson, R. A. & Kneebone, G. M. Fatty acid composition of human colostrum and mature breast milk. *Am. J. Clin. Nutr.* **34**, 252–257 (1981).
13. Grigor, M. R., Dunckley, G. G. & Purves, H. D. The synthesis of the branched-chain fatty acids of rat skin surface lipid. *Biochim. Biophys. Acta* **218**, 389–399 (1970).
14. Ran-Ressler, R. R., Devapatla, S., Lawrence, P. & Brenna, J. T. Branched chain fatty acids are constituents of the normal healthy newborn gastrointestinal tract. *Pediatr. Res.* **64**, 605–609 (2008).
15. Su, X. et al. Adipose tissue monomethyl branched-chain fatty acids and insulin sensitivity: effects of obesity and weight loss. *Obesity (Silver Spring)* **23**, 329–334 (2015).
16. Mika, A. et al. A comprehensive study of serum odd- and branched-chain fatty acids in patients with excess weight. *Obesity (Silver Spring)* **24**, 1669–1676 (2016).
17. Lackey, D. E. et al. Regulation of adipose branched-chain amino acid catabolism enzyme expression and cross-adipose amino acid flux in human obesity. *Am. J. Physiol. Endocrinol. Metab.* **304**, E1175–E1187 (2013).
18. Kishimoto, Y., Williams, M., Moser, H. W., Hignite, C. & Biermann, K. Branched-chain and odd-numbered fatty acids and aldehydes in the nervous system of a patient with deranged vitamin B12 metabolism. *J. Lipid Res.* **14**, 69–77 (1973).
19. Svensson, R. U. et al. Inhibition of acetyl-CoA carboxylase suppresses fatty acid synthesis and tumor growth of non-small-cell lung cancer in preclinical models. *Nat. Med.* **22**, 1108–1119 (2016).
20. Hiltunen, J. K. et al. Mitochondrial fatty acid synthesis type II: more than just fatty acids. *J. Biol. Chem.* **284**, 9011–9015 (2009).
21. Lewis, C. A. et al. Tracing compartmentalized NADPH metabolism in the cytosol and mitochondria of mammalian cells. *Mol. Cell* **55**, 253–263 (2014).
22. Horning, M. G., Martin, D. B., Karmen, A. & Vagelos, P. R. Fatty acid synthesis in adipose tissue. II. Enzymatic synthesis of branched chain and odd-numbered fatty acids. *J. Biol. Chem.* **236**, 669–672 (1961).
23. Oku, H., Yagi, N., Nagata, J. & Chinen, I. Precursor role of branched-chain amino acids in the biosynthesis of iso and anteiso fatty acids in rat skin. *Biochim. Biophys. Acta* **1214**, 279–287 (1994).
24. Liu, L. et al. Human fetal intestinal epithelial cells metabolize and incorporate branched chain fatty acids in a structure specific manner. *Prostaglandins Leukot. Essent. Fatty Acids* **116**, 32–39 (2017).
25. Obayashi, M. et al. Estrogen controls branched-chain amino acid catabolism in female rats. *J. Nutr.* **134**, 2628–2633 (2004).
26. Kaneda, T. *Iso- and anteiso-fatty acids in bacteria: biosynthesis, function, and taxonomic significance.* *Microbiol. Rev.* **55**, 288–302 (1991).
27. Macfarlane, G. T., Gibson, G. R., Beatty, E. & Cummings, J. H. Estimation of short-chain fatty acid production from protein by human intestinal bacteria based on branched-chain fatty acid measurements. *FEMS Microbiol. Lett.* **101**, 81–88 (1992).
28. Previs, S. F. et al. New methodologies for studying lipid synthesis and turnover: looking backwards to enable moving forwards. *Biochim. Biophys. Acta* **1842**, 402–413 (2014).
29. Abdelmagid, S. A. et al. Comprehensive profiling of plasma fatty acid concentrations in young healthy Canadian adults. *PLoS ONE*, **10**, e0116195 (2015).
30. Sailer, M. et al. Increased plasma citrulline in mice marks diet-induced obesity and may predict the development of the metabolic syndrome. *PLoS ONE*, **8**, e63950 (2013).
31. Jenkins, B. J. et al. Odd chain fatty acids; new insights of the relationship between the gut microbiota, dietary intake, biosynthesis and glucose intolerance. *Sci. Rep.* **7**, 44845 (2017).
32. Eissing, L. et al. De novo lipogenesis in human fat and liver is linked to ChREBP- β and metabolic health. *Nat. Commun.* **4**, 1528 (2013).
33. Duarte, J. A. et al. A high-fat diet suppresses de novo lipogenesis and desaturation but not elongation and triglyceride synthesis in mice. *J. Lipid Res.* **55**, 2541–2553 (2014).
34. Sanchez-Gurmaches, J. et al. Brown fat AKT2 is a cold-induced kinase that stimulates ChREBP-mediated de novo lipogenesis to optimize fuel storage and thermogenesis. *Cell Metab.* **27**, 195–209.e6 (2018).
35. Violante, S. et al. Substrate specificity of human carnitine acetyltransferase: implications for fatty acid and branched-chain amino acid metabolism. *Biochim. Biophys. Acta* **1832**, 773–779 (2013).
36. Geiger, T. et al. Initial quantitative proteomic map of 28 mouse tissues using the SILAC mouse. *Mol. Cell. Proteomics*, **12**, 1709–1722 (2013).
37. Trayhurn, P., Wang, B. & Wood, I. S. Hypoxia in adipose tissue: a basis for the dysregulation of tissue function in obesity? *Br. J. Nutr.* **100**, 227–235 (2008).
38. Robciuc, M. R. et al. VEGFB/VEGFR1-induced expansion of adipose vasculature counteracts obesity and related metabolic complications. *Cell Metab.* **23**, 712–724 (2016).
39. Ye, J., Gao, Z., Yin, J. & He, Q. Hypoxia is a potential risk factor for chronic inflammation and adiponectin reduction in adipose tissue of ob/ob and dietary obese mice. *Am. J. Physiol. Endocrinol. Metab.* **293**, E1118–E1128 (2007).
40. Mayers, J. R. et al. Tissue of origin dictates branched-chain amino acid metabolism in mutant Kras-driven cancers. *Science* **353**, 1161–1165 (2016).
41. Jang, C. et al. A branched-chain amino acid metabolite drives vascular fatty acid transport and causes insulin resistance. *Nat. Med.* **22**, 421–426 (2016).
42. Anderson, K. A. et al. SIRT4 is a lysine deacylase that controls leucine metabolism and insulin secretion. *Cell Metab.* **25**, 838–855.e15 (2017).
43. Hellerstein, M. K., Neese, R. A. & Schwarz, J. M. Model for measuring absolute rates of hepatic de novo lipogenesis and reesterification of free fatty acids. *Am. J. Physiol.* **265**, E814–E820 (1993).
44. Shin, A. C. et al. Brain insulin lowers circulating BCAA levels by inducing hepatic BCAA catabolism. *Cell Metab.* **20**, 898–909 (2014).
45. Seiler, S. E. et al. Carnitine acetyltransferase mitigates metabolic inertia and muscle fatigue during exercise. *Cell Metab.* **22**, 65–76 (2015).
46. Davies, M. N. et al. The acetyl group buffering action of carnitine acetyltransferase offsets macronutrient-induced lysine acetylation of mitochondrial proteins. *Cell Rep.* **14**, 243–254 (2016).
47. Mardinoglu, A. et al. Integration of clinical data with a genome-scale metabolic model of the human adipocyte. *Mol. Syst. Biol.* **9**, 649 (2013).
48. Kniazeva, M., Euler, T. & Han, M. A branched-chain fatty acid is involved in post-embryonic growth control in parallel to the insulin receptor pathway and its biosynthesis is feedback-regulated in *C. elegans*. *Genes Dev.* **22**, 2102–2110 (2008).
49. Yan, Y. et al. BCFA suppresses LPS induced IL-8 mRNA expression in human intestinal epithelial cells. *Prostaglandins Leukot. Essent. Fatty Acids* **116**, 27–31 (2017).
50. Ran-Ressler, R. R. et al. Branched chain fatty acids reduce the incidence of necrotizing enterocolitis and alter gastrointestinal microbial ecology in a neonatal rat model. *PLoS ONE*, **6**, e29032 (2011).

Acknowledgements

This work was supported, in part, by US National Institutes of Health (NIH) grants R01CA188652 (C.M.M.), NIH R01CA172667 (D.K.N.), P01-HL110900 (P.C.) and R01-HL126945 (P.C.), a Searle Scholar Award (C.M.M.), a Camille and Henry Dreyfus Teacher-Scholar Award (C.M.M.), an NSF CAREER Award (#1454425 to C.M.M.), and an Ajinomoto Innovation Alliance Program Grant (C.M.M.). The project was funded (in part) by a seed grant made available through the UC San Diego Larsson-Rosenquist Foundation Mother-Milk-Infant Center of Research Excellence (M.W.). J.S.G. is supported by AHA award 18CDA34080527. This material is the result of work supported with resources and the use of facilities at the VA San Diego Medical Center. The contents do not represent the views of the US Department of Veterans Affairs or the United States Government. We would like to thank M. Gantner for helping with primary brown adipose tissue isolation and culture.

Author contributions

M.W. and C.M.M. conceived and designed the study. C.R.G. carried out knock down and analysis of ACAD enzymes and assisted with design and execution of all 3T3L1 experiments; L.S.R. and D.K.N. carried out lipidomic analysis of ¹³C-traced adipocytes; and J.L.M., Y.M.L. and J.S.A. provided germ-free and SPF samples. T.P.C. and S.A.P. isolated and cultured human primary cells. N.M. and J.M.G. assisted with GC-MS analysis of in vivo samples; J.D.H. carried out gene expression

analysis of tissue samples, J.S.G. and D.A.G. carried out D₂O thermovariation experiments in mice. P.C. carried out in vivo oxygen tension and arterial blood flow studies in mice. M.W. performed all other experiments. R.L. designed and executed the clinical study of NAFL and NASH patients. M.W. and C.M.M. wrote the paper with help from all authors.

Competing interests

The authors declare no competing interests.

Additional information

Supplementary information is available for this paper at <https://doi.org/10.1038/s41589-018-0132-2>.

Reprints and permissions information is available at www.nature.com/reprints.

Correspondence and requests for materials should be addressed to C.M.M.

Publisher's note: Springer Nature remains neutral with regard to jurisdictional claims in published maps and institutional affiliations.

© The Author(s), under exclusive licence to Springer Nature America, Inc. 2018

Methods

Materials and reagents. Media and sera were purchased from Life Technologies. Glucose and amino acid isotope tracers were purchased from Cambridge Isotopes Inc. Fatty acid standards were purchased from Larodan. All other reagents were purchased from Sigma-Aldrich unless otherwise noted.

Cell culture. 3T3L1 pre-adipocytes were purchased from the American Type Culture Collection and cultured in high glucose Dulbecco's modified Eagle medium (DMEM; Life Technologies) supplemented with 10% bovine calf serum (BCS) below 70% confluence. For differentiation, cells were allowed to reach confluence (day -2), and 2 d post confluence (day 0) differentiation was induced with 0.5 mM 3-isobutyl-1-methylxanthine (IBMX), 0.25 μ M dexamethasone, and 1 μ g/ml insulin in DMEM containing 10% FBS. Media was changed on day 2 to DMEM + 10% FBS with 1 μ g/ml insulin. On day 4 and thereafter, DMEM + 10% FBS was used. Cobalamin (500 nM) was supplemented to cultures when noted. Isotope tracing was carried out 7 d post induction of differentiation unless otherwise noted. Cells were incubated in custom DMEM in which the metabolite specified was replaced with the 13 C- or 2 H-labeled version for 24 h unless otherwise specified. For short-chain fatty acid addition experiments, individual short-chain fatty acids were added to the media at the indicated concentration for 24 h, after which total fatty acids were extracted as described below. Fatty acids were then calculated as percent total fatty acids and normalized to control conditions. For LC-MS analysis of [13 C₆]valine incorporation into lipids, 3T3L1 cells were incubated in tracer media for 4 d.

BAT depots were isolated from the interscapular area of neonate mice as previously described³¹. Once cells reached confluency, differentiation was induced by addition of DMEM containing 10% FBS, 20 nM insulin, 1 nM triiodothyronine, 0.5 mM 3-isobutyl-1-methylxanthine, 2 μ g/ml dexamethasone, and 0.25 mM indomethacin for 2 d and then switched to differentiation media containing 20 nM insulin, and 1 nM triiodothyronine for 5–6 d. Isotope tracing was carried out 7 d post induction of differentiation.

Primary human white pre-adipocytes and muscle satellite cells were isolated, propagated and differentiated and then cultured for 24 h in tracer media as previously described³². Weight stable obese subjects undergoing elective laparoscopic gastric bypass via Roux-en-Y for the treatment of obesity were recruited for the study to provide material for pre-adipocyte isolation. Both human skeletal muscle biopsies and material for pre-adipocyte isolation were obtained with approval from the University of California San Diego's Committee on Human Investigation and VA San Diego Medical Center's Institutional Review Board. All donors provided informed written consent after listening to an explanation of the protocol, and the study complied with all relevant regulations.

All hypoxia experiments were carried out in a Coy hypoxia chamber, which allows media changes under hypoxic conditions. ND-646 (1,4-dihydro-1-[(2R)-2-(2-methoxyphenyl)-2-[(tetrahydro-2H-pyran-4-yl)oxy]ethyl]-a-a,5-trimethyl-6-(2-oxazolyl)-2,4-dioxothieno[2,3-d]pyrimidine-3(2H)-acetamide) was solubilized in DMSO and added to cells at a final concentration of 100 nM for 24 h in the presence of tracer.

Lipolysis assay. Differentiated 3T3-L1 adipocytes were washed twice with PBS and incubated with serum-free DMEM containing P/S, 2% FA-free BSA, and 10 μ M isoproterenol for 1 h. 100 μ L was extracted for GC-MS analysis.

Oil Red O staining. A 0.35% (w/v) Oil Red O stock was prepared in isopropanol and filtered through a 0.22 μ m filter. Cells were washed with PBS, fixed with 4% paraformaldehyde for 30 min at room temperature, washed 2 \times in milli-Q water, washed once with 60% isopropanol, and finally stained with 3:2 (stock:water) Oil Red O solution for 30 min. Stain solution was removed from cells and cells were washed 4 \times with milli-Q water before imaging.

Lentiviral production and shRNA KD of acyl CoA dehydrogenases. Glycerol stocks of TRC2-pLKO.1-puro shRNA (Supplementary Table 3) and a nontargeting control construct were purchased from Sigma-Aldrich and packaged in HEK293FT cells using the transfection agent Fugene 6 and required packaging plasmids VSV-G, gag/pol, and rev. HEK293FT medium containing lentiviral constructs was collected 2 d later and filtered (0.45 μ m). Polybrene was added to a final concentration of 6 μ g/ml. 3T3L1 pre-adipocytes were infected with 0.5 ml of virus-containing medium in a 6-well plate for 4 h before addition of 2 ml of virus-free medium. After 24 h of recovery, transduced cells were selected with 3 μ g/ml puromycin. Cells were then plated to 12-well plates for differentiation as described above. Puromycin was removed from the medium beginning on day 0 of differentiation.

Pooled CRISPR-Cas9 KO of Crat and Fasn in 3T3L1 adipocytes. Fasn, NT and CrAT target sequences (Supplementary Table 4) were cloned into the lentiCRISPRv2 plasmid (Addgene plasmid # 52961). For lentivirus production, 2–2.5 million HEK293FT cells were placed in 10-cm tissue culture plates in 10 ml of DMEM (containing 1% penicillin/streptomycin, 10% FBS). 24 h later, transfection was performed using Lipofectamine 3000 (Invitrogen) with 1.3 μ g VSV.G/PMD2.G, 5.3 μ g of lenti-gag/pol/PCMV8.2 and 4 μ g of lentiviral

vector. Lentivirus-containing supernatants were harvested 48 and 72 h later and concentrated using Amicon Ultra-15 centrifugal filters, 100,000 NMWL (Millipore) following the manufacturer's protocol. 3T3-L1 pre-adipocytes were infected with 10 μ L of virus in 1 ml of medium containing 7.5 μ g of polybrene in a 6-well plate for 4 h before addition of an extra 1 ml of virus-free medium. After 24 h of recovery, transduced cells were selected with 3 μ g/ml puromycin. Cells were then plated to 12-well plates for differentiation as described above. Puromycin was removed from the medium beginning on day 0 of differentiation.

RNA isolation and quantitative RT-PCR. Total RNA was purified from cultured cells using Trizol Reagent (Life Technologies) per the manufacturer's instructions. First-strand cDNA was synthesized from 1 μ g of total RNA using iScript Reverse Transcription Supermix for RT-PCR (Bio-Rad Laboratories) according to the manufacturer's instructions. Individual 10 μ L SYBR Green real-time PCR reactions consisted of 2 μ L of diluted cDNA, 5 μ L of SYBR Green Supermix (Bio-Rad), and 1 μ L of each 5 μ M forward and reverse primers. For standardization of quantification, 18S was amplified simultaneously. The PCR was carried out on 96-well plates on a CFX Connect Real time System (Bio-Rad) using a three-stage program provided by the manufacturer: 95 $^{\circ}$ C for 3 min, 40 cycles of 95 $^{\circ}$ C for 10 s and 60 $^{\circ}$ C for 30 s. Gene-specific primers used are listed in Supplementary Table 5. PCR data for intergene comparison were corrected for primer efficiency.

Western blots. 3T3L1 adipocytes or 100–150 mg of ground eWAT were lysed in ice-cold RIPA buffer with 1 \times protease inhibitor (Sigma-Aldrich). 30 μ g total protein was separated on a 12% SDS-PAGE gel for BCKDH blots or 20 μ g of total protein was separated on a 4–20% SDS-PAGE gel (mini-protein TGX gels, Bio-Rad) for CrAT and FASN blots. The proteins were transferred to a nitrocellulose membrane and immunoblotted with anti-Bckdha (Novus Biologicals NBP1-79616) (1:1,000 dilution), anti- β -actin (Cell Signaling 4970S) (1:5,000), anti-GAPDH (Cell Signaling 5174S), anti-CrAT (Novus NBP2-15999), anti-FASN (Proteintech 10624-2-AP). Specific signal was detected with horseradish peroxidase-conjugated secondary antibody goat anti-rabbit (1:2,500–1:10,000) using SuperSignal West Pico Chemiluminescent Substrate (Thermo Scientific) and developed using Blue Devil Autoradiography film (Genesee Scientific) or Bio-Rad Chemidoc XRS+.

Animal studies. Animal handling and care followed the NIH Guide for Care and Use of Laboratory Animals. The experimental protocols were approved by either the UCSD, Salk or UMMS Institutional Animal Care and Use Committee. C57BL/6J and ob/ob(B6.Cg-Lepob/J) were obtained from Jackson Laboratories.

Mouse fasting study. Food was removed from cages containing 12-week-old male or female C57BL/6J mice (3–4 mice per cage) at 7:00 a.m. Blood was collected via tail bleed at baseline, 2, 6, 12 and 24 h post removal of food. Mice remained in their original cage with original bedding (nonsynthetic shavings) for the duration of the experiment.

2 H₂O administration to animals. For the comparison of germ free and specific pathogen free mice, male Swiss Webster mice were bred and maintained in sterile semi-flexible isolators and screened for bacterial, viral, and fungal contamination. Age-matched male specific pathogen-free mice were used for comparison and obtained from Charles River at 5 weeks of age. Mice were maintained under a 12 h light/dark cycle and given a standard chow diet ad libitum. At 6 weeks of age, mice were subcutaneously injected with 0.035 ml/g body weight 0.9% NaCl 2 H₂O, and drinking water was replaced with 8% 2 H₂O enriched water. 8 d later, mice were fasted for 6 h (9 a.m. to 3 p.m.) and tissues collected and snap frozen in liquid N₂.

For the high-fat study, 5-week-old C57BL/6J mice were obtained from Jackson Laboratories and ad lib fed a 45% high-fat diet (D12451) or a 10% low-fat diet (D12450K) for 15 weeks from 6 weeks of age. Diets were obtained from Research Diets, Inc. 7–21 d before termination, mice were injected intraperitoneally with 0.035 ml/g body weight 0.9% NaCl 2 H₂O, and drinking water was replaced with 8% 2 H₂O-enriched water. Mice were fasted for 6 h before plasma, and tissue collection and samples were immediately snap frozen in liquid N₂.

Thermovariation experiments were carried out as previously described³⁴. Briefly, 10-week-old C57BL/6J mice were simultaneously housed in two rodent incubators (RIT33SD, Powers Scientific) within the Animal Medicine facilities of the UMMS for 4 weeks. One of them had the temperature adjusted to 30 $^{\circ}$ C (thermoneutrality group). Another incubator had its temperature decreased by four degrees weekly until reaching 6 $^{\circ}$ C, and the mice stayed at this temperature for a week (severe cold group). Room-temperature group mice were in a clean room set at 22 $^{\circ}$ C co-housed in the same facility as the mice in rodent incubators. Mouse cages were changed weekly using components pre-adjusted to temperature. Three days before termination, mice were intraperitoneally injected with 0.035 ml/g body weight 0.9% NaCl 2 H₂O (Sigma, 151882), and drinking water was replaced with 8% 2 H₂O enriched water.

Isotope labeled chow study. 5-week-old C57BL/6J mice were obtained from Jackson Laboratories and ad lib fed a custom 60% kcal high fat diet (TD.160092) or a 20% kcal fat diet (TD. 160091) for 15 weeks from 6 weeks of age. Diets and incorporated isotopes were obtained from Envigo Teklad Diets and Cambridge

isotopes, respectively. For the final 3 weeks, 25% of the total valine and leucine in the diet was replaced with [U-¹³C₅-¹⁵N]valine and [U-¹³C₆-¹⁵N]leucine so that there was 3 g [U-¹³C₅-¹⁵N]valine /100 g protein and 4 g [U-¹³C₆-¹⁵N]leucine/100 g protein in both diets. Mice were fasted overnight before plasma and tissue collection, and samples were immediately snap frozen in liquid N₂.

Tissue pO₂ and organ blood flow in HFD/LFD mice. To determine the impact of obesity on tissue pO₂, blood flow and BCKDHA levels in eWAT, 5-week-old C57BL/6J mice were obtained from Jackson Laboratories and ad lib fed a 60% kcal high fat diet (D12492) or a 10% kcal fat diet (D12450K) from research diets for 8 weeks from 6 weeks of age.

Electrodes for oxygen measurements. The oxygen partial pressure was measured using carbon fiber electrodes (Carbostar-1, Kation Scientific; Minneapolis, MN) in which the tip of the electrode was coated with 5% Nafion (Sigma; St. Louis, MO) to increase oxygen specificity. The process consisted of three individual Nafion coats. The microelectrodes were polarized at -0.8 V relative to a silver-silver chloride reference electrode (Cypress Systems; Lawrence, KS). Oxygen measurements were performed using the two electrodes system (working and reference electrode), and the current generated was measured with a potentiostat and electrometer (Keithley model 610C; Cleveland, OH). The microelectrodes were calibrated at 37 °C with 0, 5, 10 and 21% oxygen gases (Airgas; Los Angeles, CA). Tissues were superfused (0.1 ml/min) with physiological Krebs salt solution, and the tissue was maintained at 35–37 °C by the heated Krebs solution. The solution was spread on the tissue as a thin film, drained into a platter, and drawn off by suction. The solution was equilibrated with 95% N₂ and 5% CO₂, which maintained the superfusate at a pH of 7.4 and minimized O₂ delivery to the tissue from the atmosphere. Oxygen measurements were made by penetrating the tissue with the microelectrode tip. The reference electrode was placed in the bath, and the microelectrode was placed in a shielded holder and advanced toward the measurement site with a micromanipulator. A long-working distance X10 Leitz objective was used to direct the electrode to the measurement site. Before measurements, the electrode tip was immersed in the supernatant suffusion solution and the current was registered. The supernatant suffusion solution was set as 0 mm Hg reference point. Upon introduction into the tissue, the microelectrodes responded with a time constant that is estimated to be of the order of 10 s. A stable reading is obtained within 30 s, and upon reaching the current plateau value, the electrode is extracted from the tissue and the tip maintained within the suffusing saline solution.

Organ blood flow distribution. The fluorescent-labeled microsphere (FLM) method was used to determine organ blood flow. Briefly, fluorescent microspheres (Molecular Probes, Eugene, OR), 15 μm in diameter with a single color (green, yellow, red or scarlet) were suspended in saline and injected over a short 10 s period (100 μL) at the time point of interest. At the end of the protocol, animals were euthanized with a lethal dose of sodium pentobarbital, and eight vital tissues were harvested. The tissues were digested in 1 N KOH in separate containers for 24 h and then filtered. Fluorescent dye extraction was accomplished using Cellosolve (Fisher Scientific Co., Pittsburg, PA), and the number of FLMS was quantified as a function of the fluorescent signal at each specific FluoSphere wavelength (LS50B, PerkinElmer Corp., Norwalk, CT)⁵⁵.

NAFL/NASH patient sample collection. Sixteen subjects undergoing diagnostic liver biopsy for suspected NAFLD were recruited by the NAFLD Research Center at the University of California, San Diego. Subjects were carefully screened and excluded for liver diseases other than NAFLD and secondary causes of hepatic steatosis⁵⁴. Subjects drank 50 ml of 70% ²H₂O three times per day for 4 d, followed by twice a day until the date of liver biopsy, for a total period of 3–5 weeks. Plasma was collected weekly from the start of heavy water labeling until the time of biopsy. All procedures used in this study were approved by the University of California, San Diego Human Research Protections Program. Subjects provided written informed consent, and Declaration of Helsinki protocols were followed.

GC–MS analysis of fatty acids and polar metabolites. For cell culture, polar metabolites and fatty acids were extracted using methanol/water/chloroform and analyzed as previously described⁷. For tissue and plasma, metabolites and total fatty acids were extracted from tissues and plasma using a Folch-based methanol/chloroform/saline extraction at a ratio of 1:2:1 with inclusion of [³H₃₁]palmitate and norvaline as lipid and polar internal standards, respectively. Briefly, 250 μl MeOH, 500 μl CHCl₃, 250 μl saline and fatty acid isotope internal standards were added to weighed preground tissue. This was vortexed for 10 min followed by centrifugation at 10,000g for 5 min. Polar metabolites were derivatized in 2% (w/v) methoxyamine hydrochloride (Thermo Scientific) in pyridine and incubated at 37 °C for 60 min. Samples were then silylated with *N*-tertbutyldimethylsilyl-*N*-methyltri-fluoroacetamide (MTBSTFA) with 1% tert-butyl dimethylchlorosilane (tBDMS) (Regis Technologies) at 37 °C for 30–45 min. Polar derivatives were analyzed by GC–MS using a DB-35MS column (30 m × 0.25 mm i.d. × 0.25 μm, Agilent J&W Scientific) installed in an Agilent 7890 A gas chromatograph (GC) interfaced with an Agilent 5975 C mass spectrometer (MS). The lower chloroform phase was dried and then derivatized to form fatty acid methyl esters (FAMES) via

addition of 500 μl 2% H₂SO₄ in MeOH and incubation at 50 °C for 2 h. FAMES were extracted via addition of 100 μl saturated salt solution and 500 μl hexane and these were analyzed using a Select FAME column (100 m × 0.25 mm i.d.) installed in an Agilent 7890 A GC interfaced with an Agilent 5975 C MS using the following temperature program: 80 °C initial, increase by 20 °C/min to 170 °C, increase by 1 °C/min to 204 °C, then 20 °C/min to 250 °C and hold for 10 min. The percent isotopologue distribution of each fatty acid and polar metabolite was determined and corrected for natural abundance using in-house algorithms adapted from Fernandez et al.⁵⁵. The metabolite ion fragments used are summarized in Supplementary Table 6. Mole percent enrichment (MPE) was calculated via the following equation:

$$\sum_{i=1}^n \frac{M_i \cdot i}{n}$$

where n is the number of carbon atoms in the metabolite and M_i is the relative abundance of the i th mass isotopologue. Molar enrichment was determined by multiplying the MPE by the abundance.

YSI (yellow springs instrument) was used to quantify glucose, lactate, glutamine and glutamate in cell culture media.

Isotopomer spectral analysis. The contribution of oxPPP-derived NADPH to lipogenesis using the [3-³H]glucose tracer was determined via isotopomer spectral analysis (ISA) using INCA as previously described⁷. The ISA compares a measured fatty acid isotopomer distribution (determined by integrating metabolite ion fragments of fatty acids summarized in Supplementary Table 6) to one that is simulated using a reaction network for palmitate synthesis, whereby 14 NADPH molecules are consumed to form one palmitate molecule. Models were also generated for mmBCFA and OCFA synthesis, whereby 12 NADPH molecules are consumed to form one branched or odd chain fatty acid (Supplementary Tables 7 and 8). Parameters for the relative enrichment of the lipogenic NADPH pool from a given [³H] tracer and the percentage of fatty acids that are de novo synthesized are extracted from a best-fit model using INCA 4.6 metabolic flux analysis software package⁵⁶. The 95% confidence intervals for both parameters were estimated by evaluating the sensitivity of the sum of squared residuals between measured and simulated fatty acid mass isotopomer distributions to small flux variations.

GC–MS analysis of short-chain fatty acids. Cecal content was weighed, and 2 μl of water was added per mg of cecum. The sample was vortexed for 5 min and then centrifuged at 18,000g for 5 min at 10 °C. The resultant cecal water was used for SCFA analysis, and the cecal pellet was dried overnight at 60 °C to obtain the dry weight.

For cecal SCFA quantification, 50 μl of cecal water was added to a 2 ml eppendorf microcentrifuge tube, followed by 150 μl water, 10 μl 5 mM 2-ethylbutyrate, 30 μl 10 mM sodium acetate-d₃, 50 μl 1-propanol and 50 μl pyridine. The tube was placed on ice for 5 min, which was followed by addition of 100 μl 1 M NaOH and 30 μl methylchloroformate. The sample was then vortexed for 20 s followed by addition of 300 μl MTBE and then vortexed for another 20 s followed by centrifugation at 10,000g for 5 min at 4 °C. 100 μl of the upper phase was then transferred in duplicate to GC vials for analysis. Samples were analyzed by GC–MS using a DB-35MS column (30 m × 0.25 mm i.d. × 0.25 μm, Agilent J&W Scientific) installed in an Agilent 7890B gas chromatograph (GC) interfaced with an Agilent 5977B mass spectrometer (MS) using the following temperature program: 50 °C initial with a hold time of 0.8 min, followed by an increase of 25 °C/min to 120 °C and then an increase of 100 °C/min to 280 °C. Samples were injected using split mode (25 ml/min split flow), and the mass spectrometer was operated in scan mode between 50–150 AMU. Acetate was quantified from the internal acetate isotope standard and all other SCFAs were quantified from a standard curve extracted in parallel.

The isotopologue distributions of acetate and isovalerate were obtained via diethyl ether extraction and tBDMS derivatization of cecal water. Briefly, 10 μl concentrated HCl (37%) and 1 ml Et₂O was added to 100 μl cecal water, which was followed by 10 min of vortexing and centrifugation at 18,000g at 15 °C for 5 min. The upper phase was added to a new tube and the Et₂O extraction step was repeated. 250 μl of the extract was aliquoted in triplicate to GC vials, and 25 μl MTBSTFA + 1% tBDMS was added followed by incubation at room temperature for 1 h before GC–MS analysis with the following temperature program: 80 °C initial with a hold time of 0.8 min, followed by an increase of 15 °C/min to 150 °C with a hold time of 2 min, then an increase by 50 °C/min to 280 °C. Samples were injected using split mode (25 ml/min split flow) and the mass spectrometer was operated in scan mode between 50–500 AMU.

Plasma ²H₂O enrichment analysis. The ²H labeling of water from samples or standards was determined via deuterium acetone exchange. 5 μl of sample or standard was reacted with 4 μl of 10 N NaOH and 4 μl of a 5% (v/v) solution of acetone in acetonitrile for 24 h. Acetone was extracted by the addition of 600 μl chloroform and 0.5 g Na₂SO₄ followed by vigorous mixing. 100 μl of the chloroform was then transferred to a GC–MS vial. Acetone was measured using an Agilent DB-35MS column (30 m 3 0.25 mm i.d. × 0.25 μm, Agilent J&W Scientific) installed

in an Agilent 7890 A gas chromatograph (GC) interfaced with an Agilent 5975 C mass spectrometer (MS) with the following temperature program: 60 °C initial, increase by 20 °C/min to 100 °C, increase by 50 °C/min to 220 °C, and hold for 1 min. The split ratio was 40:1 with a helium flow of 1 ml/min. Acetone eluted at approximately 1.5 min. The mass spectrometer was operated in the electron impact mode (70 eV). The mass ions 58 and 59 were integrated and the percent M1 (m/z 59) calculated. Known standards were used to generate a standard curve and plasma percent enrichment was determined from this. All samples were analyzed in triplicate.

In vivo de novo lipogenesis calculations. Calculation of the fraction of newly synthesized fatty acids (FNS) was based on the method described by Lee et al.⁵⁷, where FNS is described by the following equation:

$$\text{FNS} = \frac{\text{ME}}{(n \times p)}$$

Where ME is the average number of deuterium atoms incorporated per molecule ($\text{ME} = 1 \times m_1 + 2 \times m_2 + 3 \times m_3 \dots$), p is the deuterium enrichment in water and n is the maximum number of hydrogen atoms from water incorporated per molecule. N was determined using the equation:

$$\frac{m_2}{m_1} = \frac{(n-1)}{2} \times \frac{p}{q}$$

As described by Lee et al.⁵⁷, where q is the fraction of hydrogen atoms and $p + q = 1$. The molar amount of newly synthesized fatty acids (MNS) was determined by:

$$\text{MNS} = \text{FNS} \times \text{total fatty acid amount (nmoles/mg tissue)}.$$

LC-MS lipidomic analysis. Lipid extraction was carried out using a Folch-based methanol/chloroform/saline extraction at a ratio of 1:2:1 with the inclusion of C12:0 dodecylglycerol and hexadecanoic acid- d_{31} as internal standards. The methanol phase was washed a second time with chloroform after addition of 1 μ l formic acid. Metabolite separation was achieved with a Luna reverse-phase C5 column (50 \times 4.6 mm, with 5- μ m-diameter particles; Phenomenex). Mobile phase A was composed of a 95:5 ratio of water:methanol, and mobile phase B consisted of isopropanol, methanol, and water in a 60:35:5 ratio. Solvent modifiers 0.1% formic acid with 5 mM ammonium formate and 0.1% ammonium hydroxide were used to assist ion formation and to improve the LC resolution in both positive and negative ionization modes, respectively. The flow rate for each run started at 0.1 ml/min for 5 min to alleviate backpressure associated with injecting chloroform. The gradient started at 0% B and increased linearly to 100% B over the course of 45 min with a flow rate of 0.4 ml/min, followed by an isocratic gradient of 100% B for 17 min at 0.5 ml/min before equilibrating for 8 min at 0% B with a flow rate of 0.5 ml/min. MS analysis was performed with an electrospray ionization (ESI) source on an Agilent 6430 QQQ LC-MS/MS. The capillary voltage was set to 3.0 kV, and the fragmentor voltage was set to 100 V. The drying gas temperature was 350 °C, the drying gas flow rate was 10 L/min, and the nebulizer pressure was 35 psi. Representative lipids were quantified by SRM of the transition from precursor to product ions at associated optimized collision energies as previously described⁵⁸. Briefly, for the SRM transitions in which the transition of parent masses to the loss of the headgroup (for example, loss of phosphocholine from phosphatidylcholine) is monitored, the acyl chain specificities were determined from previously described procedures⁵⁸. For phospholipids such as PCs and PEs, the fatty acid acyl chain composition was determined from phospholipids using a mobile phase containing both ammonium hydroxide and formic acid and the

fatty acid fragmentations were monitored from [M-H + HCO₂H] m/z at 40 V collision energy in negative ionization mode. For other phospholipids such as PAs and PIs, the fatty acid fragmentations from [M-H] m/z at 40 V collision energy in negative ionization mode in mobile phase containing just ammonium hydroxide were monitored. The identifying ion and the M + 4 (mass increment of 4) ion of each lipid was monitored, and relative abundance was determined by integrating the area under the curve followed by normalization to internal standard values. Significant incorporation of [¹³C]valine into lipids was determined by comparing the relative abundance of the M + 4 ion of each lipid species targeted in [¹³C₃] valine traced cells versus cells that had no tracer added (no trace) via fold change differences and Student's t -test. Percentage enrichment of each lipid species was determined via:

$$\%E = \left[\frac{{}^{13}\text{C } M_4}{{}^{13}\text{C } M_0} - \frac{{}^{12}\text{C } M_4}{{}^{12}\text{C } M_0} \right] \cdot 100$$

Where M_4 is the M + 4 abundance of each lipid, M_0 is the identifying ion abundance and ¹³C and ¹²C denote cells cultured in [¹³C₃]valine and ¹²C valine, respectively.

Statistical analysis. All results are shown as mean \pm s.e.m. P values were calculated using Student's two-tailed t -test unless otherwise specified; * P value between 0.01 and 0.05; ** P value between 0.001 and 0.01; *** P < 0.001. t -tests were carried out in GraphPad Prism, version 7. Errors associated with ISA of lipogenesis are 95% confidence intervals determined via sensitivity analysis. All cell culture experiments were replicated at least 3 independent times.

Reporting Summary. Further information on research design is available in the Nature Research Reporting Summary linked to this article.

Data availability

The data sets generated during and/or analyzed during the current study are available from the corresponding author upon reasonable request.

References

- Gantner, M. L., Hazen, B. C., Eury, E., Brown, E. L. & Kralli, A. Complementary roles of estrogen-related receptors in brown adipocyte thermogenic function. *Endocrinology* **157**, 4770–4781 (2016).
- Vacanti, N. M. et al. Regulation of substrate utilization by the mitochondrial pyruvate carrier. *Mol. Cell* **56**, 425–435 (2014).
- Cabrales, P. & Tsai, A. G. Plasma viscosity regulates systemic and microvascular perfusion during acute extreme anemic conditions. *Am. J. Physiol. Heart Circ. Physiol.* **291**, H2445–H2452 (2006).
- Decaris, M. L. et al. Identifying nonalcoholic fatty liver disease patients with active fibrosis by measuring extracellular matrix remodeling rates in tissue and blood. *Hepatology* **65**, 78–88 (2017).
- Fernandez, C. A., Des Rosiers, C., Previs, S. F., David, F. & Brunengraber, H. Correction of ¹³C mass isotopomer distributions for natural stable isotope abundance. *J. Mass. Spectrom.* **31**, 255–262 (1996).
- Young, J. D. INCA: a computational platform for isotopically non-stationary metabolic flux analysis. *Bioinformatics* **30**, 1333–1335 (2014).
- Lee, W. N. et al. In vivo measurement of fatty acids and cholesterol synthesis using D₂O and mass isotopomer analysis. *Am. J. Physiol.* **266**, E699–E708 (1994).
- Louie, S. M. et al. GSTP1 Is a driver of triple-negative breast cancer cell metabolism and pathogenicity. *Cell Chem. Biol.* **23**, 567–578 (2016).

Reporting Summary

Nature Research wishes to improve the reproducibility of the work that we publish. This form provides structure for consistency and transparency in reporting. For further information on Nature Research policies, see [Authors & Referees](#) and the [Editorial Policy Checklist](#).

Statistical parameters

When statistical analyses are reported, confirm that the following items are present in the relevant location (e.g. figure legend, table legend, main text, or Methods section).

n/a Confirmed

- The exact sample size (n) for each experimental group/condition, given as a discrete number and unit of measurement
- An indication of whether measurements were taken from distinct samples or whether the same sample was measured repeatedly
- The statistical test(s) used AND whether they are one- or two-sided
Only common tests should be described solely by name; describe more complex techniques in the Methods section.
- A description of all covariates tested
- A description of any assumptions or corrections, such as tests of normality and adjustment for multiple comparisons
- A full description of the statistics including central tendency (e.g. means) or other basic estimates (e.g. regression coefficient) AND variation (e.g. standard deviation) or associated estimates of uncertainty (e.g. confidence intervals)
- For null hypothesis testing, the test statistic (e.g. F , t , r) with confidence intervals, effect sizes, degrees of freedom and P value noted
Give P values as exact values whenever suitable.
- For Bayesian analysis, information on the choice of priors and Markov chain Monte Carlo settings
- For hierarchical and complex designs, identification of the appropriate level for tests and full reporting of outcomes
- Estimates of effect sizes (e.g. Cohen's d , Pearson's r), indicating how they were calculated
- Clearly defined error bars
State explicitly what error bars represent (e.g. SD, SE, CI)

Our web collection on [statistics for biologists](#) may be useful.

Software and code

Policy information about [availability of computer code](#)

Data collection

No software was used

Data analysis

INCA 4.6 metabolic flux analysis software package was used for ISA models and students T-tests were carried out in GraphPad Prism, version 7

For manuscripts utilizing custom algorithms or software that are central to the research but not yet described in published literature, software must be made available to editors/reviewers upon request. We strongly encourage code deposition in a community repository (e.g. GitHub). See the Nature Research [guidelines for submitting code & software](#) for further information.

Data

Policy information about [availability of data](#)

All manuscripts must include a [data availability statement](#). This statement should provide the following information, where applicable:

- Accession codes, unique identifiers, or web links for publicly available datasets
- A list of figures that have associated raw data
- A description of any restrictions on data availability

The datasets generated during and/or analyzed during the current study are available from the corresponding author upon reasonable request.

Field-specific reporting

Please select the best fit for your research. If you are not sure, read the appropriate sections before making your selection.

Life sciences Behavioural & social sciences Ecological, evolutionary & environmental sciences

For a reference copy of the document with all sections, see [nature.com/authors/policies/ReportingSummary-flat.pdf](https://www.nature.com/authors/policies/ReportingSummary-flat.pdf)

Life sciences study design

All studies must disclose on these points even when the disclosure is negative.

Sample size	For high fat and low fat dietary intervention, power analysis was carried out on changes in circulating fasting glucose levels using an alpha of 0.05 and a 1-beta of 0.95 in order to calculate the animals required.
Data exclusions	no data was excluded
Replication	all results were repeated at least 3 independent times with the exception of FASN KO where two independent infections were carried out. All attempts at replication were successful.
Randomization	Mice were assigned to groups randomly.
Blinding	Blinding was not possible as the dietary intervention caused visible differences in mouse appearance.

Reporting for specific materials, systems and methods

Materials & experimental systems

n/a	Involvement in the study
<input checked="" type="checkbox"/>	<input type="checkbox"/> Unique biological materials
<input type="checkbox"/>	<input checked="" type="checkbox"/> Antibodies
<input type="checkbox"/>	<input checked="" type="checkbox"/> Eukaryotic cell lines
<input checked="" type="checkbox"/>	<input type="checkbox"/> Palaeontology
<input type="checkbox"/>	<input checked="" type="checkbox"/> Animals and other organisms
<input type="checkbox"/>	<input checked="" type="checkbox"/> Human research participants

Methods

n/a	Involvement in the study
<input checked="" type="checkbox"/>	<input type="checkbox"/> ChIP-seq
<input checked="" type="checkbox"/>	<input type="checkbox"/> Flow cytometry
<input checked="" type="checkbox"/>	<input type="checkbox"/> MRI-based neuroimaging

Antibodies

Antibodies used	anti-BCKDHA (polyclonal, Novus Biologicals NBP1-79616, lot QC27046-42334) (1:1,000 dilution), anti-Beta-Actin (Cell Signaling 3700S, clone 8H10D10, lot 13) (1:5,000), anti-GAPDH (Cell signaling 5174S, clone D16H11, lot 4), anti-CrAT (polyclonal, Novus NBP2-15999, lot 40177), anti-FASN (polyclonal, Proteintech 10624-2-AP, LOT 00039886).
Validation	Antibodies for western blotting were validated for mouse reactivity by previous publications (BCKDHA, eg. PMID: 26571352, Beta-Actin, e.g. PMID: 14702115 GAPDH, e.g. PMID: 29620171, CrAT e.g. PMID: 29350465) and/or the manufacturer (Beta-Actin, GAPDH, FASN) as listed (publications) or shown (manufacturer western blot) directly on the manufacturers website.

Eukaryotic cell lines

Policy information about [cell lines](#)

Cell line source(s)	3T3L1 cells from ATCC
Authentication	Cell line was not authenticated following purchase from ATCC.
Mycoplasma contamination	Cell culture was tested for mycoplasma and confirmed negative.
Commonly misidentified lines (See ICLAC register)	No commonly misidentified cell lines were used.

Animals and other organisms

Policy information about [studies involving animals](#); [ARRIVE guidelines](#) recommended for reporting animal research

Laboratory animals	Animal handling and care followed the NIH Guide for Care and Use of Laboratory Animals. The experimental protocols were approved by either the UCSD, Salk or UMMS Institutional Animal Care and Use Committee. C57BL/6J, ob/ob(B6.Cg-Lepob/J) and swiss webster mice were used in this study. All males were used with the exception of female C57BL/6J which were used for a male female comparison.
Wild animals	This study did not involve wild animals.
Field-collected samples	The study did not involve samples collected from the field.

Human research participants

Policy information about [studies involving human research participants](#)

Population characteristics	For the NAFLD study, all procedures were approved by the University of California–San Diego Human Research Protections Program. Subjects provided written informed consent, and Declaration of Helsinki protocols were followed. Subjects were carefully screened and excluded for liver diseases other than NAFLD and secondary causes of hepatic steatosis. Eight males and eight females were in the study group with an age and BMI range of 31-70 and 27-40. Weight stable obese subjects undergoing elective laparoscopic gastric bypass via Roux-en-Y for the treatment of obesity were recruited for the study to provide material for pre-adipocyte isolation and skeletal muscle biopsy. Both human skeletal muscle biopsies and material for pre-adipocyte isolation were obtained with approval from the University of California San Diego's Committee on Human Investigation and VA San Diego Medical Center's Institutional Review Board. All donors provided informed written consent after listening to an explanation of the protocol and the study complied with all relevant regulations.
Recruitment	Subjects were recruited while undergoing diagnostic liver biopsy for suspected NAFLD. Subjects were recruited for pre-adipocyte isolation and muscle biopsy while undergoing elective laparoscopic gastric bypass via Roux-en-Y for the treatment of obesity.